Asymmetric spread of excitatory synaptic potential in hippocampal neuronal dendrites revealed by voltage imaging

Masato Morita[1], Reo Higashi[1], Shin-ya Kawaguchi[1,*]

[1]Department of Biophysics, Graduate School of Science, Kyoto University, Kitashirakawa Oiwake-cho, Sakyo-ku, Kyoto 606-8502, Japan

*Correspondence

Corresponding author: Shin-ya Kawaguchi,

e-mail: kawaguchi.shinya.7m@kyoto-u.ac.jp

tel: +81-75-753-4200

Keywords

voltage imaging, hippocampal neuron, dendrite, excitatory postsynaptic potential (EPSP), local computation

SUMMARY

Despite intensive studies for decades on synaptic integration in the somatodendritic compartments, its spatio-temporal dynamics remains obscure because of the technical limitation to obtain local potentials at multiple subcellular regions. To address this issue, here we used a genetically-encoded voltage indicator together with local uncaging of glutamate or GABA on cultured hippocampal pyramidal neurons. Fluorescence voltage imaging revealed direction-dependent opposite changes of excitatory postsynaptic potentials (EPSPs) in a dendrite: EPSPs attenuated during propagation toward the soma whereas amplified toward the distal branch end. The direction-dependent local augmentation of EPSPs was mediated by the TTX-resistant Na^+ channels and KCC2-dependent deeper dendritic resting potential than in soma, the latter of which was directly unveiled by subcellular patch-clamp recordings from a thin dendrite hundreds μm away from the soma. Taken all these results together, our data identifies an asymmetric modulation of excitatory signals in neuronal dendrites, potentially impacting local integration in a branch.

INTRODUCTION

Neurons extend elaborate dendrites to receive synaptic inputs from other neurons. These synaptic inputs are spatially and temporally integrated in an analogue manner, and then the signals are transformed into action potentials (APs) as digital all-or-none signals at the axon initial segment. It has been shown that hippocampal and cortical pyramidal neurons exhibit several types of regenerative local spikes upon synaptic inputs in dendrites, including Na^+, NMDA, and Ca^{2+} spikes.[1,2] Na^+ and NMDA spikes are triggered by local multiple synaptic inputs in dendritic branches.[3,4,5,6] On the other hand, Ca^{2+} spikes mediated by voltage-gated Ca^{2+} channels, show larger and broader waveforms, often leading to burst APs.[1,7,8] In contrast to such a dendritic supra-linear computation mediated by active conductances, sub-threshold potential changes are thought to obey the passive membrane properties of dendrites, attenuating during the propagation as the cable theory predicts.[9,10] However, at present, it remains elusive how the subthreshold potential changes are processed in dendrite because of the difficulty to apply the patch-clamp technique to multiple points of a thin dendrite at the same time. As a corollary, mathematical model of electrical circuit assuming multiple compartments has provided basic view of signal integration in dendrites,[11,12] which still remains to be consolidated by direct experimental analysis.

53 In this decade, genetically-encoded voltage indicators (GEVIs), which detect
54 membrane potential changes as fluorescence changes, have drastically
55 developed.[13,14,15] This technique has enabled to fluorescently detect membrane potential
56 changes at a tiny structure which is difficult to apply the patch-clamp technique, for
57 example even a dendritic spine and a presynaptic bouton.[16,17] Taking advantage of the
58 leading-edge voltage imaging technique, in this study, we studied how synaptic potentials
59 are processed in dendrites. Using improved version of ASAP1 (Accelerated Sensor of
60 Action Potentials 1),[13] a fluorescent voltage imaging probe, expressed in a cultured
61 hippocampal neuron in combination with very local glutamate or GABA stimulation on a
62 dendrite by 405 nm spot-laser-mediated photoactivation, we found that glutamatergic
63 PSPs spread in dendrites with opposite modulation depending on the direction of
64 propagation. We also identified a novel Cl^--dependent mechanism underlying the unique
65 asymmetric processing of the electrical signal in dendrites.
66
67
68 **RESULTS**
69 ***Fluorescent imaging of membrane potential changes in a cultured hippocampal***
70 ***neuron***

To improve voltage imaging probe ASAP1[13] for higher sensitivity to membrane potential changes, some of amino acid replacements reported in an improved version ASAP3[18] were introduced into ASAP1 (here we note this version ASAP3β; for details, see methods). We evaluated fluorescence change of ASAP3β upon voltage changes by expressing in HEK293T cells (Figure S1A). ASAP3β exhibited fluorescence decrease (-40.0 ± 1.1 % ΔF/F, Figures S1B and S1C) in response to 100 mV depolarization of the voltage-clamped HEK293T cell from a holding potential at -70 mV, which corresponded to almost two-fold sensitivity of the original ASAP1 (-18.5 ± 1.2 % ΔF/F, Figure S1C) similarly to ASAP3.[18]

We then examined how ASAP3β detects neuronal activity characterized by rapid membrane potential changes in a cultured hippocampal neuron by expressing it with electroporation (Figure 1A). Both the fluorescence and the membrane potential were simultaneously recorded by imaging and patch-clamp methods. ASAP3β detected spontaneous excitatory postsynaptic potentials (EPSPs) almost perfectly without any noticeable change in time course (Figure 1B), showing ~ 1 % fluorescence change for 2 mV membrane potential change (Figure 1C). On the other hand, more rapid spontaneous or evoked APs were detected as smaller fluorescence changes relative to the actual change of membrane potential (-8.4 ± 0.4 % ΔF/F upon 93.6 ± 2.7 mV, Figures 1B and

89 1C), likely because of the insufficient velocity of ASAP3β to follow a given rapid voltage

90 change (Figures 1B and 1C). From these observations, it was confirmed that ASAP3β

91 nicely detects synaptic potentials.

92

93 ***Direction-dependent EPSP modulation in dendrites***

94 Taking advantage of real-time fluorescent detection of local membrane potential changes

95 of interest throughout dendritic arborization, we studied how synaptic potentials

96 propagate in dendrites. Glutamatergic EPSPs were evoked by local photo-activation of

97 MNI-caged-glutamate (300 μM in the external bath) by 405 nm laser illumination (2 μm

98 diameter) at a spine of ASAP3β-expressing hippocampal pyramidal neuron in culture

99 (Figure 1D). Simultaneous recordings of membrane potentials by current-clamp and

100 fluorescent imaging from an ASAP3β-expressing neuron showed similar waveforms of

101 EPSPs characterized by ~ 1.2 % fluorescence change at the soma upon 2 mV potential

102 change without temporal lag (Figure 1D). Thus, evoked EPSP (eEPSP) measurement

103 by ASAP3β enabled us to quantify the spatial pattern of EPSP spreading in a neuron.

104 Using this method, eEPSPs were monitored as the relative ASAP fluorescence

105 changes (ΔF/F) throughout the dendrites of ASAP3β-expressing hippocampal neurons

106 in the view field (Figures 1E and 1F). In line with the prediction of the cable theory,[11] the

107 fluorescence change for eEPSP ($\Delta F/F_{eEPSP}$) attenuated as propagation toward the soma

108 (Figures 1E and 1G). The $\Delta F/F_{eEPSP}$ decreased by 25 ± 2 % at 33.6 ± 3.1 μm away from

109 the uncaged site and by 59 ± 3 % at 97.7 ± 4.9 μm (Figure 1H, black circles). Thus, the

110 propagation of EPSPs toward the soma attenuates almost exponentially as

111 characterized by a length constant of ~ 145 ± 20 μm. In contrast, surprisingly, EPSPs

112 detected as $\Delta F/F_{eEPSP}$ rather amplified when propagating toward the distal end of a

113 dendritic branch (Figures 1E-1H). The $\Delta F/F_{eEPSP}$ increased by 21 ± 4 % at 54.7 ± 1.9 μm

114 away from the uncaged site and by 23 ± 3 % at 110.6 ± 4.5 μm (Figure 1H, red), although

115 variable. This is quite contrasting to the classical view of passive traveling of

116 subthreshold membrane potential changes in a cable, in which membrane potential

117 change attenuates during propagation in a dendritic tree regardless of direction. The

118 $\Delta F/F_{eEPSP}$ amplification detected by ASAP imaging during propagation toward the distal

119 end was not dependent on the absolute size of $\Delta F/F_{eEPSP}$ at the uncaged site (ranging

120 from 1.1 % to 10.9 %) that reflects the magnitude of EPSPs (Figures 1I and S1D). Thus,

121 our data indicated that excitatory synaptic inputs are oppositely modulated in a dendrite

122 depending on the direction of propagation.

123 In our self-customized fluorescent imaging system, the LED illumination is designed to

124 be assembled around the center of view field so that high fluorescent signal is attained

as possible even for a very fast image acquisition. As a result, the absolute fluorescent signals around the edge of view field tended to be smaller, potentially giving rise to a tendency for the signal to noise ratio to become lower at those dimmer regions. To test whether the different intensity of light illumination affects the $\Delta F/F_{eEPSP}$ amplification in the distal end, we compared $\Delta F/F_{eEPSP}$ signals at identical points of dendrite obtained in two distinct view fields by moving the microscope. As shown in Figure S2, spatial pattern of $\Delta F/F_{eEPSP}$ signals in dendrites was little affected by the relative brightness of fluorescence.

The above results indicated that excitatory synaptic signals amplify during propagation toward the distal dendrite from the input site. We wondered whether this amplification of depolarization takes place specifically at the only branch where EPSP was evoked or broadly occurs also at distal branches irrespective of the location of glutamate uncaging. To examine this, we analyzed how eEPSP propagates into branches stemming out of the bifurcation on the way to soma from the uncaged site (Figure S3). Some branches exhibited $\Delta F/F_{eEPSP}$ augmentation during propagation toward distal dendrites compared to the signal at the branch points (Figure S3), suggesting that the EPSP amplification during propagation toward distal dendrites was not necessarily limited to the stimulated branch. On the other hand, other branches exhibited gradual attenuation of

143 depolarization even when traveling toward the distal end (Figure S3). These apparently
144 contrasting results imply that not all the branches are equipped with the amplification of
145 depolarization, which would be responsible for the diverse extent of the $\Delta F/F_{eEPSP}$
146 amplification even at the stimulated branch as shown in Figure 1H.
147

148 ***TTX-resistant Na^+ channels underlie EPSP amplification in distal dendrites***

149 To explore the molecular mechanisms of the EPSP amplification in distal dendrites,
150 several ion channels were blocked by pharmacological agents. Voltage-gated Na^+
151 channels (Na_V) are known to be present in dendrites of pyramidal neurons,[19] contributing
152 to backpropagation of spikes.[20] First, we applied a typical Na_V blocker, tetrodotoxin (TTX,
153 1 μM) to the external bath, and examined $\Delta F/F_{eEPSP}$ propagation by ASAP3β imaging
154 (Figure 2A). The EPSP amplification in distal dendrite was not affected by TTX ($\Delta F/F_{eEPSP}$
155 amplification, 1.32 ± 0.05, Figures 2A, 2C and 2D). While TTX is a typical Na_V blocker
156 used for inhibition of Na^+ spikes, TTX-resistant Na^+ channels, such as $Na_V1.5$, 1.8 and
157 1.9, are also known. Among these, at least $Na_V1.5$ and $Na_V1.9$ are reported to be
158 expressed in hippocampal pyramidal neurons.[21,22,23] In the presence of lidocaine (5 mM),
159 which broadly inhibits Na_V, the $\Delta F/F_{eEPSP}$ amplification in distal dendrites was not
160 significant ($p = 0.25$, paired t-test, Figures 2B and 2C), although slight augmentation was

161 still remaining ($\Delta F/F_{eEPSP}$ amplification, 1.12 ± 0.05, Figure 2D). Thus, TTX-resistant Na^+

162 channels might partially underlie the EPSP amplification in distal dendrites.

163 We next examined the possible involvement of other cation channels and glutamate

164 receptors in the EPSP amplification in distal dendrites. Voltage-gated Ca^{2+} channels and

165 NMDA receptors are reported to produce dendritic Ca^{2+} and NMDA spikes upon

166 glutamatergic synaptic inputs, contributing to subcellular local computation by

167 supralinear synaptic integration.[6,24] Neither external administration of Cd^{2+} (Ca^{2+} channel

168 blocker, 100 μM, Figure 3A) nor D-AP5 (NMDA receptor antagonist, 100 μM, Figure 3B)

169 affected the $\Delta F/F_{eEPSP}$ amplification during propagation toward distal dendrites,

170 suggesting that Ca^{2+} channels and NMDA receptors are not involved in the EPSP

171 amplification here we are focusing on (Figure 3D). In addition, inhibition of

172 hyperpolarization-activated cation channels (HCN channels) and inward rectifier K^+

173 channels (IRK channels) by application of blockers, ZD7288 and Ba^{2+}, respectively, failed

174 to affect the $\Delta F/F_{eEPSP}$ amplification (Figures 3D and S4). Taken all these results together,

175 it is suggested that the positive-feedback activation of TTX-resistant Na^+ channels by

176 depolarization may specifically, but partly, contribute to the $\Delta F/F_{eEPSP}$ amplification in

177 distal dendrites.

178 To confirm the above idea, we next attempted to disturb the positive-feedback

179 activation of Na_V by reducing membrane resistance through shunting effect mediated by

180 tonic activation of $GABA_A$ receptors ($GABA_ARs$). As expected, increased shunting effect

181 by external GABA (50 μM) completely abolished the direction-dependent augmentation

182 of $\Delta F/F_{eEPSP}$ ($\Delta F/F_{eEPSP}$ amplification, 0.91 ± 0.05; p = 0.0016, Dunnett's test; Figures 3C

183 and 3D). Thus, it is concluded that the $\Delta F/F_{eEPSP}$ amplification depends on the positive-

184 feedback activation of depolarizing system composed of the TTX-resistant Na^+ channels

185 among voltage-gated conductances.

186

187 ***GABAergic PSPs attenuate as spread in dendrites irrespective of direction***

188 To further study the spatial pattern of spreading of membrane potential changes in a

189 dendrite, we examined how GABAergic postsynaptic potentials (PSP_{GABA}s) spread in

190 dendrites by the ASAP3β imaging coupled with local activation of $GABA_ARs$. PSP_{GABA}s

191 were caused by local uncaging of DPNI-caged-GABA (200-500 μM) with a spot 405 nm

192 laser illumination (Figures 4 and S5), in a similar manner to the local glutamate

193 stimulation. In most cases, local GABA stimulation on a dendrite of hippocampal neuron

194 exhibited little fluorescence change of ASAP3β, reflecting the resting membrane

195 potential (Vm_{rest}) close to the equilibrium potential for Cl^- (E_{Cl}). Some cells exhibited

196 increase of ASAP3β fluorescence upon GABA uncaging, corresponding to

197 hyperpolarization (Figures 4A and S5A). In contrast, only very limited cases showed
198 depolarization as observed with fluorescence decrease upon the local GABA, which is
199 probably caused by somehow high internal Cl^- ($[Cl^-]_{in}$) (Figures 4B and S5B). In any cases,
200 PSP_{GABA}s were not amplified during the propagation in both directions of dendrites
201 (Figures 4 and S5), which was a sharp contrast to the asymmetric modulation of
202 glutamatergic EPSPs (see Figure 1). This discrepancy in the signal processing between
203 glutamate- and GABA-caused depolarizations made us to assume that the Cl^-
204 conductance and/or E_{Cl} might play a role in amplification of local depolarization in a distal
205 dendritic branch.
206
207 ***Low $[Cl^-]_{in}$-dependent deeper Vm_{rest} in distal dendrites***
208 It is determined by the difference between E_{Cl} and local Vm_{rest} whether $GABA_A$Rs exert
209 depolarization or hyperpolarization. Therefore, we attempted to measure Vm_{rest} in
210 dendrites of hippocampal neurons. For that aim, a direct patch-clamp recording from a
211 thin dendrite was performed using the EGFP-fluorescence as a guide to precisely target
212 the pipette (Figures 5A and 5B). Whole-cell current-clamp recording showed that,
213 surprisingly, the Vm_{rest} was more negative in a dendrite (-75.6 ± 1.5 mV) than in the soma
214 (-68.3 ± 1.4 mV, p = 0.019, Tukey test, Figure 5C). When the dendritic Vm_{rest} was plotted

against the distance from the soma, there was a tendency for Vm_{rest} to become more negative in a distal dendrite (-3.5 mV / 100 μm, Figure 5D). In addition to the deeper Vm_{rest}, leak conductance per membrane area size (measured at -70 mV under the voltage-clamp configuration) became higher in a dendrite farther away from the soma (Figure 5E), suggesting that more leak channels are basally open at the distal dendrite compared to the soma.

Taken the above results together, we hypothesized that the deeper Vm_{rest} in a distal branch might be related to the Cl^- conductance and/or homeostasis depending on the location. This idea was tested using VU0463271 (10 μM), an inhibitor of KCC2, a type of Cl^- transporter which predominantly contributes to the low $[Cl^-]_{in}$ in mature neurons.[25] Immunocytochemistry exhibited more abundant expression of KCC2 in distal dendrites of hippocampal pyramidal neurons than in the soma (1.5-fold, $p = 0.019$, Tukey test, Figures 5F and 5G). KCC2 basically establishes low $[Cl^-]_{in}$ by excluding Cl^- out of the cytoplasm, and VU0463271 is expected to bring about higher $[Cl^-]_{in}$. When KCC2 was inhibited, the Vm_{rest} in a dendrite became higher by ~ 6 mV, while the somatic Vm_{rest} was not affected, resulting in almost identical potentials at dendrites and soma (dendrite: -66.5 ± 2.0 mV, soma: -67.9 ± 1.9 mV, Figures 5C and 5D). On the other hand, the tendency of higher basal leak conductance at the distal dendrite was not affected by the

233 disruption of low $[Cl^-]_{in}$ (Figure 5E). These results altogether suggested that the lower

234 $[Cl^-]_{in}$ and/or higher Cl^- conductance in a dendrite than in the soma could be a potential

235 cause for the deeper Vm_{rest} in dendrites.

236

237 ***EPSP amplification relies on the low $[Cl^-]_{in}$ in dendrites***

238 Based on the above results, we considered that the specific $[Cl^-]_{in}$ regulation and/or the

239 resultant deeper Vm_{rest} in distal dendrites compared with the soma might play a role in

240 the local $\Delta F/F_{eEPSP}$ amplification. Accordingly, in the presence of VU0463271 (10 μM), a

241 glutamatergic eEPSP monitored by the ASAP3β imaging tended to exhibit smaller

242 amplification in distal dendrites ($\Delta F/F_{eEPSP}$ amplification, 1.09 ± 0.03; p = 0.019, Dunnett's

243 test, Figures 6A and 6C), implying the involvement of low $[Cl^-]_{in}$ in the dendritic

244 amplification of EPSPs. Moreover, simultaneous inhibition of Na_V and KCC2 by lidocaine

245 and VU0463271 almost abolished the $\Delta F/F_{eEPSP}$ amplification ($\Delta F/F_{eEPSP}$ amplification,

246 1.04 ± 0.03; p = 0.004, Dunnett's test, Figures 6B and 6C). Taken all these data together,

247 it is suggested that the low $[Cl^-]_{in}$ in distal dendrites is a critical factor for the EPSP

248 amplification in distal dendrites together with TTX-resistant Na^+ channels.

249

250 ***Role of Cl^- channels in the low Vm_{rest} and local EPSP amplification***

251 Finally, we attempted to understand how Cl^- contributes to the local augmentation of
252 EPSP spreading in the distal dendrite. Taking the following 2 facts into account: 1), the
253 distal dendritic branch exhibits deeper Vm_{rest} and higher basal leak conductance (see
254 Figure 5); 2), the local augmentation of PSP size is specific to the depolarization
255 mediated by Na^+ but not by Cl^- (see Figures 1 and 4), we speculated that the Cl^-
256 conductance at the distal dendrite might be responsible for the higher leak conductance
257 which could bring the Vm_{rest} closer to E_{Cl}. Among Cl^- channels, hippocampal pyramidal
258 neurons express ClC-2[26] (Figure 7A), which is hyperpolarization-activated and regulates
259 Cl^- homeostasis and membrane excitability.[27,28] Thus, it might be possible that more likely
260 ClC-2 activation by the deeper Vm_{rest} in a distal dendrite would increase the basal Cl^- leak
261 conductance, that tends to make the Vm_{rest} closer to the E_{Cl} which is kept deep by the
262 powerful action of KCC2 locally (Figure 7B). To test this hypothesis, we constructed a
263 biophysical simple model assuming hyperpolarization-activated Cl^- conductance like
264 ClC-2 (see Methods for detail of model). When an excitatory input (brief increase of
265 conductance with a reversal potential at 0 mV) is given, an EPSP-like depolarization is
266 caused, and importantly, the depolarization became larger during the traveling toward a
267 region with enriched hyperpolarization-activated Cl^- conductances like ClC-2 (Figures
268 7C-7E). This local augmentation of depolarization in the model was suppressed either

by the elimination of sensitivity of Cl^- conductances to hyperpolarization or by the reduction of a depolarization-caused Na_V activation (Figures 7D and 7E). Even when the synaptic input site is altered, the local EPSP amplification was evident at distal branches although the extent of augmentation was variable (Figure 7E), in line with the variable amplification in actual distal branches (see Figure 1). Thus, our simple model supported the idea that the two voltage-sensitive conductances synergistically contribute to the local EPSP augmentation at distal branches. Accordingly, ASAP3β imaging experiment showed that the inhibition of Cl^- conductances by NPPB (50 μM), a blocker of relatively broad types of Cl^- channels including ClC-2, applied together with the Na_V inhibitor lidocaine strongly suppressed the local augmentation of eEPSP in a distal dendrite (Figure 7F). Thus, our simulation of EPSP traveling in a cable equipped with 2 positive-feedback mechanisms, depolarization-activated Na^+ conductance and hyperpolarization-activated Cl^- conductance, nicely predicted the cooperative action of those mechanisms to locally augment the excitatory synaptic signals, which was confirmed by the experiment.

Direction-dependent spatio-temporal integration of synaptic inputs array

Neuronal dendrites spatio-temporally integrate inputs at numerous synapses.

287 Considering our data that glutamatergic synaptic inputs asymmetrically spread in a
288 dendritic tree depending on the direction of propagation, we speculated that the synaptic
289 integration might be affected by the asymmetric modulation of synaptic inputs.
290 Hippocampal pyramidal neurons receive inputs from entorhinal cortex (EC) directly via
291 perforant path (or temporo-ammonic path) at distal apical dendrites, and indirectly via
292 the tri-synaptic circuit (mossy fibers or Schaffer collaterals) at the proximal region.[29]
293 Based on such a circuit organization, in a certain situation, excitatory signals may arrive
294 at an apical dendrite of a single cell with a spatio-temporal context: from distal to proximal,
295 which might have a specific impact on synaptic summation. To test this idea, distinct
296 temporal orders of glutamate photolysis were performed at multiple locations along a
297 branch (10 sites, 35 ms intervals) in the presence of TTX (1 μM). We compared the
298 effects of three different patterns of eEPSP trains: laser spots were illuminated along a
299 branch, (1) in a sequence from the soma toward the end (to distal, a to j, Figure 8A), (2)
300 in a sequence from the end of a branch toward the soma (to soma, j to a, Figure 8A),
301 and (3) at random. Fluorescent imaging of ASAP3β showed that the $\Delta F/F_{eEPSP}$ at distal
302 region (ROI_{distal}, Figure 8A) was larger than that either at the uncaged branch or at
303 proximal region ($ROI_{proximal}$) in all three spatio-temporal patterns of stimuli (Figure 8B).
304 Thus, $\Delta F/F_{eEPSP}$ upon multiple stimuli on a branch is augmented during the propagation

305 toward the distal end of dendrite, in consistent with the data for single eEPSPs. In
306 addition, the location-dependent $\Delta F/F_{eEPSP}$ amplification was weakened by application of
307 lidocaine (5 mM) and VU0463271 (10 μM) (Figure S6A), but not by Cd^{2+} (100 μM) and
308 D-AP5 (100 μM) (Figure S6B). Notably, peak of $\Delta F/F_{eEPSP}$ by 10 uncagings became
309 smaller either by lidocaine & VU0463271 or Cd^{2+} & D-AP5, compared with the control
310 (Figures 8C and S6C), indicating synergistic actions of several positive feedback
311 mechanisms to enhance the multiple excitatory inputs for spatio-temporal summation in
312 dendrites.

313 Furthermore, pyramidal neuronal dendrites exhibited distinct augmentation of EPSP
314 summation depending on the spatio-temporal order of synaptic activation. Although the
315 $\Delta F/F_{eEPSP}$ at ROI_{distal} reached similar peaks in two conditions, “to soma” and “to distal”
316 (Figures 8D and S6D, $p > 0.05$, paired t-test), the signal at a distal branch (ROI_{distal})
317 steeply summated during glutamate uncagings in a sequence of “to soma” compared to
318 “to distal” (Figure 8D, $p < 0.01$, two-way ANOVA), but not at a proximal branch ($ROI_{proximal}$,
319 Figure S6E). The ratio of the eEPSP train trace (at ROI_{distal}) for “to soma” divided by that
320 for “to distal”, reflecting the preference of “to soma” direction for effective summation of
321 excitatory inputs, was kept higher than 1 during the EPSP array (Figure 8E). Importantly,
322 such an efficient synaptic summation was clearly weakened by lidocaine & VU0463271

(Figure 8D, $p > 0.05$, two-way ANOVA; and Figure 8E, $p < 0.01$, two-way ANOVA). Thus, the Na_V- and low $[Cl^-]_{in}$-dependent $\Delta F/F_{eEPSP}$ amplification seems to make it possible for a distal branch to distinguish the spatio-temporal pattern of synaptic inputs, resulting in local computation in a distinct manner.

DISCUSSION

In this study, using voltage imaging with a genetically-encoded probe ASAP3β combined with local glutamate or GABA uncaging, subcellular patch-clamp recordings, and biophysical model simulation, we explored how glutamatergic and GABAergic synaptic inputs propagated in hippocampal neuronal dendrites. Imaging analysis of membrane potential changes at multiple dendritic branches demonstrated direction-dependent asymmetric propagation of excitatory synaptic inputs in a dendrite, that is, EPSPs attenuated during propagation toward the soma, while amplified toward the distal end. Moreover, the EPSP amplification depended on synergistic actions of TTX-resistant Na^+ channels and low $[Cl^-]_{in}$-related Cl^- conductance. Thus, the data presented in this study showed asymmetric modulation of glutamatergic synaptic inputs in contrast to the conventional view established from the classical cable theory: subthreshold membrane potential changes gradually attenuate during spreading in dendrites. Together, our

341 findings provide a novel concept of local modulation of synaptic integration in a single
342 neuron.
343
344 ***Fluorescent voltage imaging***
345 To examine the spatio-temporal propagation pattern of synaptic inputs, we used
346 fluorescent voltage imaging with a GEVI. Patch-clamp electrophysiology has been a
347 powerful technique to precisely record electrical signals at a given position in a neuron,
348 although it requires a sophisticated technique. On the other hand, GEVIs enable us to
349 measure membrane potential changes much more easily even from multiple subcellular
350 regions at the same time, that is very difficult to perform by conventional patch-clamp
351 recordings. In this decade, several types of GEVI, including ASAP,[13] have been
352 developed, such as ArcLight,[30] Ace2N-mNeon,[14] Voltron,[31] and so on.[15,32] Taking
353 advantage of this merit, recent studies applied GEVIs to various preparations *in vivo* and
354 *in vitro,* demonstrating neuronal excitability changes dependent on behavioral states in
355 animals.[32] Moreover, GEVIs could be non-invasive compared with whole-cell patch-
356 clamp recordings which is typically accompanied with washout of cytoplasmic
357 components. As demonstrated in this study, $[Cl^-]_{in}$ is critical for the local EPSP
358 amplification (see Figures 5-7). We speculate that monitoring of membrane potential

without intracellular dialysis must have been essential for the evaluations of such cellular functions. Therefore, the lack of useful technique like voltage imaging based on GEVIs must have veiled the asymmetric EPSP amplification at a distal dendrite.

Modulation of synaptic potentials in dendrites

Previous studies have suggested local augmentation of synaptic inputs by active conductances via voltage-gated cation channels such as Na^+ and/or Ca^{2+} channels and NMDA receptors.[4,6,24,33] Notably, such augmentation of local excitatory inputs emerges when the input size is relatively large (~ 5 mV or larger when recorded at the soma). On the other hand, the EPSP amplification in distal dendrites demonstrated here operates even if the amplitude of EPSP is small (estimated to be locally 2 ~ 3 mV). Together, the EPSP amplification mediated by the voltage-dependent Na^+ and Cl^- conductances demonstrated in this study would complementarily function together with other active conductances which operate in a relatively depolarized situation, to locally enhance membrane potential changes in a relatively wide working range.

Supralinear synaptic integration in the local dendrite dependent on the active conductances has been shown in hippocampal and cortical pyramidal neurons,[5,6] whereas other types of neurons such as dentate gyrus granule cells and cerebellar

377 interneurons, show linear or sublinear summation.[34,35,36] Thus, processing of synaptic
378 inputs in dendrites seems diverse in distinct types of neurons. Different thickness and/or
379 branch pattern of dendrites, in addition to different combinations of voltage-gated
380 channels, in distinct types of neurons might define the processing pattern. Hippocampal
381 cultured neuronal preparation used here contains several types of neurons such as
382 pyramidal cells, granule cells and inhibitory interneurons. Among them we here focused
383 on pyramidal cells which clearly exhibited the asymmetric EPSP modulation in dendrites
384 (see Figure 1), while apparent granule cells didn't show such amplification (not shown).
385 Thus, distinct neuronal types seem equipped with specific machinery for local
386 computation in dendrites.

387 Asymmetric propagation of EPSPs may play a role in associative establishment of
388 synaptic plasticity such as long-term potentiation or depression. Previous studies
389 demonstrated that EPSPs caused at a dendrite sequentially in the direction toward the
390 soma, likely caused an AP firing in cortical pyramidal neurons.[37] Furthermore, the long-
391 term plasticity at excitatory synapses tends to be induced by clustered inputs at a
392 dendritic region compared to distributed inputs,[38] and dendritic spike firing in a distal thin
393 branch is likely to induce the long-term potentiation.[38,39] Here we demonstrated, as
394 shown in Figure 8, that the asymmetric EPSP modulation mechanism clearly enhanced

395 the amplitude of EPSPs train at a distal branch depending on the spatio-temporal context
396 of inputs, which potentially raises the probability of cooperative induction of plasticity in
397 a limited dendritic branch. Thus, asymmetric modulation of EPSPs revealed here might
398 associate a given pattern of EPSPs arriving at a distal dendrite, contributing to the local
399 dendritic spikes and long-term plasticity. Hippocampal pyramidal neurons receive inputs
400 from various regions: For example, CA3 pyramidal neurons are innervated from
401 perforating fibers in stratum lacunosum-moleculare, mossy fibers in stratum lucidum, and
402 associational connections in stratum radiatum.[40,41] The local asymmetric modulation of
403 excitatory synaptic inputs would provide selective summation of such specific synaptic
404 inputs at local area of dendrite.
405
406 ***Molecular mechanism for the EPSP amplification in distal dendrites***
407 This study identified an unique mechanism of local augmentation of excitatory synaptic
408 inputs in a distal dendrite: low $[Cl^-]_{in}$- and Cl^- conductance-dependent enhancement of
409 depolarization in distal dendrites (see Figures 5-7). Our biophysical model simulation
410 indicated that a type of Cl^- channel, ClC-2, could constitute a kind of positive-feedback
411 loop to stably keep the membrane potential negative closer to the E_{Cl} depending on the
412 channel property of hyperpolarization-mediated opening. In such a situation, a

413 depolarization could decrease the Cl^- conductance, which indirectly contributes to the
414 enhancement of propagating depolarizing responses (see Figure 7). Indeed, the direct
415 subcellular patch-clamp recordings of dendritic branches demonstrated the low $[Cl^-]_{in}$-
416 dependent deeper Vm_{rest} and higher leak conductances at distal branches in a distance-
417 dependent manner from the soma (see Figure 5). It is intriguing that such a Cl^--
418 dependent mechanism to augment the depolarizing responses works together with some
419 TTX-resistant Na^+ channels. In this study, we could not present data directly showing the
420 specific involvement of ClC-2 channels in the asymmetric EPSP modulation because of
421 the lack of specific blockers. The direct confirmation of the responsible Cl^- channels is
422 an important task to be accomplished in a future study.

423 In addition to the involvement of ClC-2-like Cl^- conductance, distinct E_{Cl} may also be
424 present at distal dendrites contributing to deeper Vm_{rest} there. Previous patch-clamp
425 recordings suggested that E_{Cl} at dendrites may deeper than that at the soma because of
426 the lower $[Cl^-]_{in}$ which is established by KCC2 activity.[42,43,44,45] More abundant expression
427 of KCC2 in spines and vicinity of spines[43,46] and/or more efficient Cl^- extrusion by KCC2
428 might operate at distal dendrites based on the distinct surface/volume ratio, as shown by
429 Báldi et al.[47] in hippocampal pyramidal cells. Furthermore, regulation of KCC2 by
430 phosphorylation and dephosphorylation in distal dendrites[42,48,49] may also give rise to

431 diverse modes of Cl^- homeostasis, potentially impacting the local processing of synaptic
432 potentials in a branch.

433 Our data demonstrated asymmetric propagation of glutamatergic EPSPs, whereas
434 symmetric propagation of depolarizing PSP_{GABA}s (see Figures 1 and 4). Depolarizing
435 PSP_{GABA}s would have been caused by high $[Cl^-]_{in}$. In such a case, like in the presence of
436 VU0463271 (see Figure 5), E_{Cl} should be higher and the deep Vm_{rest} at a distal dendrite
437 would also be absent, which precludes one of the two critical positive-feedback
438 mechanisms for the EPSP amplification.

439 In addition to the $[Cl^-]_{in}$-mediated dynamic control of membrane potential, TTX-resistant
440 Na^+ channels were demonstrated to underlie in the local EPSP amplification here.
441 Among three subtypes of TTX-resistant Na^+ channels, $Na_V1.5$, 1.8 and 1.9,[50] $Na_V1.9$ is
442 especially activated at more negative membrane potential (-70 ~ -60 mV).[51] eEPSPs
443 caused here by spot laser illumination on a spine, was not so large in amplitude: ranging
444 from ~ 1 % to 10 % $\Delta F/F$, corresponding to from 2 mV depolarization to ~ 20 mV at most.
445 The typical activation of Na_V is emerging from -40 ~ -50 mV, which would make other
446 subtypes unlikely to be involved in the EPSP amplification. Thus, distinct subtypes of
447 Na_V with different activation profile might provide neurons an ability to operate in a unique
448 manner to locally compute the voltage signals.

ACKNOWLEDGMENTS

We thank to Drs. M. Midorikawa and T. Inoshita for critical reading of the manuscript and helpful comments. This work was supported by JSPS/MEXT KAKENHI Grant Numbers JP22H02721 and JP22K19360 (SK), the Takeda Science Foundation (SK), the Naito Foundation (SK), and Grant-in-Aid for JSPS Fellows Grant Numbers JP22J14296 and JP22KJ1851 (MM).

AUTHOR CONTRIBUTIONS

MM performed most imaging and patch-clamp experiments and data analysis; RH performed simulation and analysis; SK conceptualized and administrated the study; SK and MM interpreted data and wrote the manuscript. All authors approved the final version.

DECLARATION OF INTERESTS

The authors declare no competing interests.

464 **EXPERIMENTAL MODEL AND SUBJECT DETAILS**

465 *HEK293T cells*

466 HEK293T cells were cultured at 37 °C in humidified air containing 5 % CO_2 in DMEM
467 (Nakalai Tesque, Kyoto, Japan) supplemented with 10 % (v/v) FBS (NICHIREI
468 BIOSCIENCES, Tokyo, Japan) and penicillin (100 U/mL)-streptomycin (0.1 mg/mL,
469 Nakalai Tesque). For testing voltage-dependent fluorescence changes, HEK293T cells
470 were transfected with original ASAP1 or modified-ASAP (ASAP3β) using Lipofectamine
471 3000 (1 μg DNA, 2 μL P3000 reagent, 1.5 μL Lipofectamine for 35 mm dish; Thermo
472 Fisher Scientific, Waltham, MA, USA).

473

474 *Hippocampal neuron culture and transfection*

475 The animals were maintained and treated according to the NIH guide for the care and
476 use of laboratory animals, and to the ethical guidelines on animal experimentation of
477 Kyoto University. Hippocampi were dissected out from male and female newborn Wistar
478 rats and incubated in Ca^{2+} and Mg^{2+}-free Hank's balanced salt solution (CMF-HBSS)
479 containing 0.1 % trypsin for 5 min at 37 °C. Neurons were dissociated by trituration with
480 a fire-polished Pasteur pipette and seeded on poly-D-lysine (Sigma-Aldrich, St. Louis,
481 MO, USA)-coated glasses in Neurobasal plus medium containing 2 % B27 plus

482 supplement (Thermo Fisher Scientific) and penicillin (100 U/mL)-streptomycin (0.1
483 mg/mL, Nakalai Tesque). Some cells were transfected with plasmids by means of
484 electroporation with NEPA21 (Nepa Gene, Chiba, Japan). 1×10^6 cells were mixed with
485 plasmids (6 μg ASAP3β plasmid or 3 μg pCAsalEGFP[52]) in 100 μL CMF-HBSS. Square
486 electric pulses were applied at 300 V (pulse length, 0.5 ms; two pulses; interval, 50 ms;
487 voltage decay rate, 10 %), followed by additional pulses at 20 V (pulse length, 50 ms;
488 five pulses; interval, 50 ms; voltage decay rate, 40 %; polarity exchanged pulse).
489 Transfected cells were then cultured on the glasses together with the non-treated ones.
490 The cells were cultured at 37 °C in humidified air containing 5 % CO_2. One day after
491 seeding, 75 % of the medium was replaced with fresh one. Since then, half of the medium
492 was replaced every 4 days.
493
494 **METHOD DETAILS**
495 *Plasmid construction*
496 Plasmids were constructed by standard molecular biology techniques. The coding DNA
497 for ASAP1 was obtained from Addgene (#52519), and some modifications for higher
498 voltage sensitivity (D145Δ, L146G, S147T, N149R, S150G, and H151D) in an improved
499 version ASAP3[18] were introduced by PCR-mediated mutations. Modified-ASAP

500 (ASAP3β) or original ASAP1 cDNAs was inserted into the vector made from pAAV-MSC
501 by replacement of CMV promotor and beta-globin intron region by CA promotor and
502 intron region from pCAGGS, followed by insertion of WPRE sequence before hGH pA
503 region.
504
505 *Electrophysiology*
506 Whole-cell voltage-clamp recording from an ASAP-expressing HEK293T cell was
507 performed with an amplifier (EPC10; HEKA Elektronik GmbH, Reutlingen, Germany) in
508 an extracellular solution containing (in mM) 145 NaCl, 5 KOH, 2 $CaCl_2$, 1 $MgCl_2$, 10
509 Hepes and 10 glucose (pH 7.3) at room temperature (20-24 °C). Patch pipettes (3-5 MΩ)
510 were filled with an internal solution containing (in mM) 147 CsCl, 5 EGTA, 10 Hepes, 15
511 CsOH, 2 ATP, 0.2 GTP (pH 7.3). The membrane potential (a holding potential of -70 mV)
512 was changed by step voltage depolarizations and hyperpolarizations to a voltage (-100
513 mV to 50 mV) for 30 ms.
514 In recordings from hippocampal neurons in culture for 2-3 weeks, we used an
515 extracellular solution containing (in mM) 120 NaCl, 5 KOH, 2 $CaCl_2$, 1 $MgCl_2$, 10 Hepes
516 and 10 glucose (pH 7.3). Patch pipettes (3-5 MΩ, somatic recordings; 20-25 MΩ,
517 dendritic recordings) were filled with an internal solution containing (in mM) 120 K-

518 gluconate, 7 KCl, 5 EGTA, 10 Hepes, 2 ATP, 0.2 GTP (pH 7.3 adjusted with KOH). In
519 some experiments, TTX (1 μM, FUJIFILM Wako Pure Chemical Corporation, Tokyo,
520 Japan), lidocaine (5 mM, Nakalai Tesque), D-AP5 (100 μM, Tocris Bioscience, Bio-
521 Techne SRL, Minneapolis, MN, USA), Cd^{2+} (100 μM, FUJIFILM Wako Pure Chemical
522 Corporation), ZD7288 (100 μM, Tocris bioscience), Ba^{2+} (30 μM, Nakalai Tesque),
523 VU0463271 (10 μM, Tocris Bioscience) and NPPB (50 μM, Tocris Bioscience) were used
524 to inhibit Na^{+} channels, NMDA receptors, Ca^{2+} channels, HCN channels, IRK channels,
525 KCC2 and Cl^{-} channels, respectively. GABA (50 μM, Nakalai Tesque) was used to
526 activate $GABA_A$ receptors.
527
528 *Fluorescent imaging*
529 Fluorescence imaging was performed using an inverted microscope IX71 (Olympus,
530 Tokyo, Japan) through a 40× 0.95-NA objective (Olympus) for HEK293T cells, or a 60×
531 1.42-NA oil-immersion objective (Olympus) for hippocampal neurons. Fluorescent
532 excitation was delivered using a white LED (SOLA; Lumencor, OR, USA) with 15
533 mW/mm^2 through a 450-480 nm filter. Fluorescent images were obtained with a Zyla4.2
534 sCMOS camera (Andor Technology Ltd, Belfast, UK) at 1500 Hz (128 × 128 pixels,
535 binning 2 × 2) for HEK293T cells, at 400 Hz (512 × 512 pixels, binning 2 × 2) or at 200

536 Hz (1392 × 1040 pixels, binning 2 × 2) for hippocampal neurons and analyzed with SOLIS

537 (Andor) or Image J software (NIH, Bethesda, MD, USA).

538

539 *Glutamate or GABA uncaging*

540 For glutamate or GABA uncaging, MNI-caged-L-glutamate (300 μM, Tocris Bioscience)

541 or DNPI-caged-GABA (200-500 μM, Tocris Bioscience) was applied to the external

542 solution. Uncaging was caused by 405 nm laser illumination (Single line laser; Rapp

543 OptoElectronic GmbH, Wedel, Germany) with 4-6 mW laser power.[53,54] Glutamate

544 uncaging was performed by laser illumination at a 2 μm diameter spot (0.2 ms duration;

545 or 1 ms in the presence of external GABA), while GABA was uncaged by a spot or a line

546 scan (0.5-5 ms duration). The location of laser illumination was controlled by a localized

547 photomanipulation system based on Galvano mirrors (UGA-42 Firefly; Rapp

548 OptoElectronic) implemented in SysCon software (Rapp OptoElectronic).

549

550 *Immunocytochemistry*

551 Cultured neurons were fixed with 4 % paraformaldehyde in phosphate buffered saline,

552 permeabilized with 0.5 % Tween 20, then blocked with 1 % goat serum, and finally

553 labeled with primary and secondary antibodies. The following antibodies were used:

554 rabbit polyclonal antibodies (pAb) against KCC2 (1:1000, Sigma-Aldrich), ClC-2 (1:5000,
555 Alomone Labs, Jerusalem, Israel), chicken pAb against GFP (1:2000, Sigma-Aldrich),
556 Alexa 568-conjugated pAb against rabbit IgG (1:400, Thermo Fisher Scientific) and Alexa
557 488-conjugated pAb against chicken IgG (1:400, Thermo Fisher Scientific). Fluorescent
558 images were recorded with a confocal laser microscope (FV1000 imaging system,
559 Olympus, Japan), and analyzed using ImageJ software (NIH). The neuronal dendrites
560 were defined as the area positive for GFP.
561

562 *Simulation of simple dendrite model with voltage-dependent Na^+ and Cl^- channels*

563 Simple model of a dendrite equipped with the depolarization-activated Na_V and the
564 hyperpolarization-activated Cl^- channels was constructed and simulated using the
565 *NEURON* simulator[55] version 8.2 operating under the Python programming language.
566 Here we assumed a multi-compartment model consisting of a soma and 18 dendritic
567 sections with single branch point where 3 daughter branches stemmed out (see Figure
568 7C), one of which had 120 μm and the other two 90 μm in length, yielding total
569 arborization length of 500 or 470 μm long. The diameter of a dendritic branch was
570 assumed to be 2.5 μm at the most proximal one, narrowing down towards the distal end
571 until it reaches 0.5 μm at 200 μm away from the soma. Cytosolic resistivity was here set

572 at 250 Ω·cm, and membrane capacitance 0.8 μF/cm^2. Membrane of individual
573 compartments were equipped with TTX-resistant voltage-gated Na^+ channel $Na_V1.9$,
574 hyperpolarization-activated Cl^- channel like ClC-2, Na^+/K^+ pump, KCC2, and linear leak
575 conductances for Na^+, K^+, and Cl^- (for detailed parameters of each components, see
576 Table S1).

577 Individual components in each compartment at the membrane potential (V_m) were
578 expressed in the model based on the equilibrium potentials for Na^+ (E_{Na}), K^+ (E_K), and
579 Cl^- (E_{Cl}) by implementing the equations which were already published in previous studies,
580 as described below.

581

582 For TTX-resistant persistent Na channels, $Na_V1.9$ model[56] was here used:

583 $$I_{Nav} = \overline{g_{Nav}} \times m_{Nav} \times h_{Nav} \times (V_m - E_{Na})$$

584 , where $\overline{g_{Nav}}$, m_{Nav}, h_{Nav} are the maximal conductance, voltage-dependent activation and
585 inactivation probability factors, respectively. Voltage-dependent changes of m_{Nav} and h_{Nav}
586 were defined by the rate constants (α and β) as described by the following equations:

587 $$\frac{dm_{Nav}}{dt} = \alpha_{m_{Nav}} \times (1 - m_{Nav}) - \beta_{m_{Nav}} \times m_{Nav}$$

588 $$\frac{dh_{Nav}}{dt} = \alpha_{h_{Nav}} \times (1 - h_{Nav}) - \beta_{h_{Nav}} \times h_{Nav}$$

589 , where forward (α) and reverse (β) rate constants for m_{Nav} and h_{Nav} were assumed as

below:

$$\alpha_{m_{Nav}} = \frac{1.032}{1 + \exp\left(\frac{V_m + 6.99}{-14.87115}\right)}$$

$$\beta_{m_{Nav}} = \frac{5.79}{1 + \exp\left(\frac{V_m + 130.4}{22.9}\right)}$$

$$\alpha_{h_{Nav}} = \frac{0.06435}{1 + \exp\left(\frac{V_m + 73.26415}{3.71928}\right)}$$

$$\beta_{h_{Nav}} = \frac{0.13496}{1 + \exp\left(\frac{V_m + 10.27853}{-9.09334}\right)}$$

For hyperpolarization-activated Cl^- component, a modified biophysical model for ClC-2[57] was incorporated:

$$I_{Cl} = \bar{g}_{Cl} \times m_{Cl} \times (V_m - E_{Cl})$$

$$\frac{dm_{Cl}}{dt} = 0.1 \times \left(m_{Cl,ss} - m_{Cl}\right)$$

, where $\bar{g}_{Cl}$ is the maximal conductance, m_{Cl} is the relative open probability factor of the channel, and its steady state at V_m, $m_{Cl,ss}$ is defined as:

$$m_{Cl,ss} = \frac{1}{1 + \exp\left(\frac{V_m - E_{Cl} + V_h}{V_s}\right)}$$

, where V_h and V_s are parameters to define the voltage-sensitivity of the channel activation.

For KCC2, K^+ and Cl^- fluxes were calculated as a product of the parameter for its anti-

porting efficiency (U_{KCC2}) and the difference between their equilibrium potentials as demonstrated in Gentiletti et al.[58]:

$$I_{K(KCC2)} = U_{KCC2} \ln\left(\frac{[K^+]_{in}[Cl^-]_{in}}{[K^+]_{out}[Cl^-]_{out}}\right)$$

$$I_{Cl(KCC2)} = -I_K$$

Na^+/K^+ pump activity was calculated based on the formulations in Takeuchi et al.,[59] as listed below,

$$I_{NaK} = I_{NaKmax}\big(k_1 \times p_{E1Na} \times y - 0.04 \times p_{E2Na} \times (1-y)\big)$$

$$I_{K(pump)} = -2I_{NaK}$$

$$I_{Na(pump)} = 3I_{NaK}$$

State transitions of the pump were defined by rate constants as below:

$$\frac{dy}{dt} = \alpha_y(1-y) - \beta_y y$$

$$\alpha_y = 0.04 \times p_{E2Na} + 0.165 \times p_{E2K}$$

$$\beta_y = \frac{0.37}{1 + \frac{0.094}{[ATP]_{in}}} \times p_{E1Na} + 0.01 \times p_{E1K}$$

$$[\mathrm{Na}^+]_{eff} = [\mathrm{Na}^+]_{out} \exp\left(-\frac{0.82 \times 96.4853 \times V_m}{8.314463 \times T}\right)$$

$$p_{E1Na} = \left(1 + \left(\frac{4.05}{[\mathrm{Na}^+]_{in}}\right)^{1.06}\left(1 + \frac{[K^+]_{in}}{32.88}\right)^{1.12}\right)^{-1}$$

$$p_{E1K} = \left(1 + \left(\frac{32.88}{[\mathrm{K}^+]_{in}}\right)^{1.12}\left(1 + \frac{[\mathrm{Na}^+]_{in}}{4.05}\right)^{1.06}\right)^{-1}$$

$$p_{E2Na} = \left(1 + \left(\frac{69.8}{[\mathrm{Na}^+]_{eff}}\right)^{1.06}\left(1 + \frac{[K^+]_{out}}{0.258}\right)^{1.12}\right)^{-1}$$

623 $$p_{E2K} = \left(1 + \left(\frac{0.258}{[\mathrm{K}^+]_{out}}\right)^{1.12} \left(1 + \frac{[\mathrm{Na}^+]_{eff}}{69.8}\right)^{1.06}\right)^{-1}$$

624 In our model, calculation of the Na^+/K^+ pump activity was specifically implemented in

625 Neuron simulator, by modifying the program code presented in Botta et al.[60]

626

627 Notably, here we assumed the hyperpolarization-activated Cl^- channels only at distal

628 compartments (see Figure 7C). An EPSP was represented as a double exponential

629 conductance change (reversal potential at 0 mV) at a single compartment (#6-8 in Figure

630 7C), defined by the rise and decay time constants of 10 and 80 ms, respectively, and the

631 peak conductance was optimized to cause similar size of EPSP (~ 12 mV) at the

632 stimulated compartment. The model was simulated in *Neuron* platform with backward

633 Euler method (dt = 0.025 ms). In some simulations to evaluate the role of the voltage-

634 dependent Na_V and Cl^- conductances in the model, the maximal conductance of Na_V was

635 halved and/or the Cl^- conductances at distal branches were set constant.

636

637

638 **QUANTIFICATION AND STATISTICAL ANALYSIS**

639 *Data analysis of ASAP fluorescence change*

640 Dendritic regions were selected for analysis as ROIs in ImageJ, and F_{dend} was calculated

641 as the mean intensity of fluorescence in each ROI which was subtracted by background

642 noise defined as the mean of fluorescence intensity at the area nearby each ROI. During

643 image acquisition of ASAP-expressing cells, fluorescence gradually decreased due to

644 photobleaching, which was defined as F_{base} obtained by double exponential curve fitting

645 of the total fluorescence change as follows:

646 $$F_{base} = A + B \cdot \exp\{\alpha \cdot (-t/\tau_1) + (1-\alpha) \cdot (-t/\tau_2)\}$$

647 All above parameters (A, B, α, τ_1 and τ_2) were determined by the least square method

648 from the time course of fluorescence change before the uncaging. The relative change

649 of fluorescence ($\Delta F/F$, %) was

650 $$\Delta F/F = (F_{dend} / F_{base} - 1) \cdot 100$$

651 In this study, relative fluorescence change of ASAP is represented as $-\Delta F/F$ because of

652 the negative relation of fluorescence against membrane potential change. $-\Delta F/F$ traces

653 in individual ROIs were obtained by averages of 3-7 trials. Adjacent area to the laser spot

654 was excluded from analysis because of an artifact by laser illumination. Distance

655 between two sites of interest was measured using ImageJ (NIH).

656

657 *Statistics analysis*

658 Statistical significance of differences between groups was tested by paired Student's t-

659 test, Dunnett's test, Tukey test or two-way ANOVA, and $P < 0.05$ was considered as

660 significant. Throughout the project, data are presented as mean ± standard error of the

661 mean (SEM) unless otherwise stated. In all figures, symbols with error bars indicate

662 mean ± SEM; asterisk, $P < 0.05$; double asterisk, $P < 0.01$; triple asterisk, $P < 0.001$.

663 These analyses were performed by Microsoft Excel and Igor Pro8 (WaveMetrics, Lake

664 Oswego, OR, USA).

Reference

1. Stuart, G.J., and Spruston, N. (2015). Dendritic integration: 60 years of progress. Nat Neurosci *18*, 1713−1721. 10.1038/nn.4157.

2. Higley, M.J., and Sabatini, B.L. (2008). Calcium Signaling in Dendrites and Spines: Practical and Functional Considerations. Neuron *59*, 902–913. 10.1016/j.neuron.2008.08.020.

3. Ariav, G., Polsky, A., and Schiller, J. (2003). Submillisecond Precision of the Input-Output Transformation Function Mediated by Fast Sodium Dendritic Spikes in Basal Dendrites of CA1 Pyramidal Neurons. J. Neurosci. *23*, 7750 − 7758. 10.1523/JNEUROSCI.23-21-07750.2003.

4. Losonczy, A., and Magee, J.C. (2006). Integrative Properties of Radial Oblique Dendrites in Hippocampal CA1 Pyramidal Neurons. Neuron *50*, 291 − 307. 10.1016/j.neuron.2006.03.016.

5. Branco, T., and Häusser, M. (2011). Synaptic Integration Gradients in Single Cortical Pyramidal Cell Dendrites. Neuron *69*, 885−892. 10.1016/j.neuron.2011.02.006.

6. Makara, J.K., and Magee, J.C. (2013). Variable Dendritic Integration in Hippocampal CA3 Pyramidal Neurons. Neuron *80*, 1438−1450. 10.1016/j.neuron.2013.10.033.

7. Golding, N.L., Jung, H., Mickus, T., and Spruston, N. (1999). Dendritic Calcium Spike Initiation and Repolarization Are Controlled by Distinct Potassium Channel Subtypes in CA1 Pyramidal Neurons. J. Neurosci. *19*, 8789−8798. 10.1523/JNEUROSCI.19-20-08789.1999.

8. Williams, S.R., and Stuarty, G.J. (1999). Mechanisms and consequences of action potential burst firing in rat neocortical pyramidal neurons. The Journal of Physiology *521*, 467−482. 10.1111/j.1469-7793.1999.00467.x.

9. Golding, N.L., Mickus, T.J., Katz, Y., Kath, W.L., and Spruston, N. (2005). Factors mediating powerful voltage attenuation along CA1 pyramidal neuron dendrites: Voltage attenuation in CA1 dendrites. The Journal of Physiology *568*, 69 −

82. 10.1113/jphysiol.2005.086793.

10. Nevian, T., Larkum, M.E., Polsky, A., and Schiller, J. (2007). Properties of basal dendrites of layer 5 pyramidal neurons: a direct patch-clamp recording study. Nat Neurosci *10*, 206−214. 10.1038/nn1826.

11. Rall, W. (1967). Distinguishing theoretical synaptic potentials computed for different soma-dendritic distributions of synaptic input. Journal of Neurophysiology *30*, 1138–1168. 10.1152/jn.1967.30.5.1138.

12. Tran-Van-Minh, A., Cazé, R.D., Abrahamsson, T., Cathala, L., Gutkin, B.S., and DiGregorio, D.A. (2015). Contribution of sublinear and supralinear dendritic integration to neuronal computations. Front. Cell. Neurosci. *9*. 10.3389/fncel.2015.00067.

13. St-Pierre, F., Marshall, J.D., Yang, Y., Gong, Y., Schnitzer, M.J., and Lin, M.Z. (2014). High-fidelity optical reporting of neuronal electrical activity with an ultrafast fluorescent voltage sensor. Nat Neurosci *17*, 884−889. 10.1038/nn.3709.

14. Gong, Y., Huang, C., Li, J.Z., Grewe, B.F., Zhang, Y., Eismann, S., and Schnitzer, M.J. (2015). High-speed recording of neural spikes in awake mice and flies with a fluorescent voltage sensor. Science *350*, 1361–1366. 10.1126/science.aab0810.

15. Xu, Y., Zou, P., and Cohen, A.E. (2017). Voltage imaging with genetically encoded indicators. Current Opinion in Chemical Biology *39*, 1−10. 10.1016/j.cbpa.2017.04.005.

16. Kwon, T., Sakamoto, M., Peterka, D.S., and Yuste, R. (2017). Attenuation of Synaptic Potentials in Dendritic Spines. Cell Reports *20*, 1100 − 1110. 10.1016/j.celrep.2017.07.012.

17. Hoppa, M.B., Gouzer, G., Armbruster, M., and Ryan, T.A. (2014). Control and Plasticity of the Presynaptic Action Potential Waveform at Small CNS Nerve Terminals. Neuron *84*, 778–789. 10.1016/j.neuron.2014.09.038.

18. Villette, V., Chavarha, M., Dimov, I.K., Bradley, J., Pradhan, L., Mathieu, B., Evans, S.W., Chamberland, S., Shi, D., Yang, R., et al. (2019). Ultrafast Two-Photon Imaging of a High-Gain Voltage Indicator in Awake Behaving Mice. Cell *179*, 1590-

1608.e23. 10.1016/j.cell.2019.11.004.

19. Remy, S., Beck, H., and Yaari, Y. (2010). Plasticity of voltage-gated ion channels in pyramidal cell dendrites. Current Opinion in Neurobiology *20*, 503–509. 10.1016/j.conb.2010.06.006.

20. Stuart, G.J., and Sakmann, B. (1994). Active propagation of somatic action potentials into neocortical pyramidal cell dendrites. Nature *367*, 69–72. 10.1038/367069a0.

21. Blum, R., Kafitz, K.W., and Konnerth, A. (2002). Neurotrophin-evoked depolarization requires the sodium channel NaV1.9. Nature *419*, 687–693. 10.1038/nature01085.

22. Jeong, S.-Y., Goto, J., Hashida, H., Suzuki, T., Ogata, K., Masuda, N., Hirai, M., Isahara, K., Uchiyama, Y., and Kanazawa, I. (2000). Identification of a Novel Human Voltage-Gated Sodium Channel α Subunit Gene, SCN12A. Biochemical and Biophysical Research Communications *267*, 262–270. 10.1006/bbrc.1999.1916.

23. Zhou, Y., Luo, Z., Bi, F., Li, J., and Xiao, B. (2019). Expression of Nav1.5 in the pathogenesis of temporal lobe epilepsy. Cell Mol Biol (Noisy-le-grand) *65*, 58–62. 10.14715/cmb/2019.65.2.9.

24. Yang, S., Emiliani, V., and Tang, C.-M. (2014). The kinetics of multibranch integration on the dendritic arbor of CA1 pyramidal neurons. Front. Cell. Neurosci. *8*. 10.3389/fncel.2014.00127.

25. Liu, R., Wang, J., Liang, S., Zhang, G., and Yang, X. (2020). Role of NKCC1 and KCC2 in Epilepsy: From Expression to Function. Front. Neurol. *10*, 1407. 10.3389/fneur.2019.01407.

26. Sík, A., Smith, R.L., and Freund, T.F. (2000). Distribution of chloride channel-2-immunoreactive neuronal and astrocytic processes in the hippocampus. Neuroscience *101*, 51–65. 10.1016/S0306-4522(00)00360-2.

27. Staley, K., Smith, R., Schaack, J., Wilcox, C., and Jentsch, T.J. (1996). Alteration of GABAA Receptor Function Following Gene Transfer of the CLC-2 Chloride Channel. Neuron *17*, 543–551. 10.1016/S0896-6273(00)80186-5.

28. Rinke, I., Artmann, J., and Stein, V. (2010). ClC-2 Voltage-Gated Channels Constitute Part of the Background Conductance and Assist Chloride Extrusion. J. Neurosci. *30*, 4776−4786. 10.1523/JNEUROSCI.6299-09.2010.

29. Stepan, J., Dine, J., and Eder, M. (2015). Functional optical probing of the hippocampal trisynaptic circuit in vitro: network dynamics, filter properties, and polysynaptic induction of CA1 LTP. Frontiers in Neuroscience *9*. 10.3389/fnins.2015.00160.

30. Jin, L., Han, Z., Platisa, J., Wooltorton, J.R.A., Cohen, L.B., and Pieribone, V.A. (2012). Single Action Potentials and Subthreshold Electrical Events Imaged in Neurons with a Fluorescent Protein Voltage Probe. Neuron *75*, 779 − 785. 10.1016/j.neuron.2012.06.040.

31. Abdelfattah, A.S., Kawashima, T., Singh, A., Novak, O., Liu, H., Shuai, Y., Huang, Y.-C., Campagnola, L., Seeman, S.C., Yu, J., et al. (2019). Bright and photostable chemigenetic indicators for extended in vivo voltage imaging. Science *365*, 699–704. 10.1126/science.aav6416.

32. Adam, Y., Kim, J.J., Lou, S., Zhao, Y., Xie, M.E., Brinks, D., Wu, H., Mostajo-Radji, M.A., Kheifets, S., Parot, V., et al. (2019). Voltage imaging and optogenetics reveal behaviour-dependent changes in hippocampal dynamics. Nature *569*, 413 − 417. 10.1038/s41586-019-1166-7.

33. Losonczy, A., Makara, J.K., and Magee, J.C. (2008). Compartmentalized dendritic plasticity and input feature storage in neurons. Nature *452*, 436 − 441. 10.1038/nature06725.

34. Krueppel, R., Remy, S., and Beck, H. (2011). Dendritic Integration in Hippocampal Dentate Granule Cells. Neuron *71*, 512−528. 10.1016/j.neuron.2011.05.043.

35. Abrahamsson, T., Cathala, L., Matsui, K., Shigemoto, R., and DiGregorio, D.A. (2012). Thin Dendrites of Cerebellar Interneurons Confer Sublinear Synaptic Integration and a Gradient of Short-Term Plasticity. Neuron *73*, 1159−1172. 10.1016/j.neuron.2012.01.027.

36. Tran-Van-Minh, A., Abrahamsson, T., Cathala, L., and DiGregorio, D.A. (2016). Differential Dendritic Integration of Synaptic Potentials and Calcium in Cerebellar Interneurons. Neuron *91*, 837−850. 10.1016/j.neuron.2016.07.029.

37. Branco, T., Clark, B.A., and Häusser, M. (2010). Dendritic Discrimination of Temporal Input Sequences in Cortical Neurons. Science *329*, 1671 − 1675. 10.1126/science.1189664.

38. Magó, Á., Weber, J.P., Ujfalussy, B.B., and Makara, J.K. (2020). Synaptic Plasticity Depends on the Fine-Scale Input Pattern in Thin Dendrites of CA1 Pyramidal Neurons. J. Neurosci. *40*, 2593−2605. 10.1523/JNEUROSCI.2071-19.2020.

39. Weber, J.P., Andrásfalvy, B.K., Polito, M., Magó, Á., Ujfalussy, B.B., and Makara, J.K. (2016). Location-dependent synaptic plasticity rules by dendritic spine cooperativity. Nat Commun *7*, 11380. 10.1038/ncomms11380.

40. Ishizuka, N., Weber, J., and Amaral, D.G. (1990). Organization of intrahippocampal projections originating from CA3 pyramidal cells in the rat. J. Comp. Neurol. *295*, 580−623. 10.1002/cne.902950407.

41. Ishizuka, N., Cowan, W.M., and Amaral, D.G. (1995). A quantitative analysis of the dendritic organization of pyramidal cells in the rat hippocampus. J. Comp. Neurol. *362*, 17−45. 10.1002/cne.903620103.

42. Chamma, I., Heubl, M., Chevy, Q., Renner, M., Moutkine, I., Eugène, E., Poncer, J.C., and Lévi, S. (2013). Activity-Dependent Regulation of the K/Cl Transporter KCC2 Membrane Diffusion, Clustering, and Function in Hippocampal Neurons. J. Neurosci. *33*, 15488−15503. 10.1523/JNEUROSCI.5889-12.2013.

43. Gauvain, G., Chamma, I., Chevy, Q., Cabezas, C., Irinopoulou, T., Bodrug, N., Carnaud, M., Lévi, S., and Poncer, J.C. (2011). The neuronal K-Cl cotransporter KCC2 influences postsynaptic AMPA receptor content and lateral diffusion in dendritic spines. Proc. Natl. Acad. Sci. U.S.A. *108*, 15474−15479. 10.1073/pnas.1107893108.

44. Khirug, S., Huttu, K., Ludwig, A., Smirnov, S., Voipio, J., Rivera, C., Kaila, K., and Khiroug, L. (2005). Distinct properties of functional KCC2 expression in immature mouse

hippocampal neurons in culture and in acute slices: Regulation of KCC2 in immature hippocampal neurons. European Journal of Neuroscience *21*, 899−904. 10.1111/j.1460-9568.2005.03886.x.

45. Khirug, S., Yamada, J., Afzalov, R., Voipio, J., Khiroug, L., and Kaila, K. (2008). GABAergic Depolarization of the Axon Initial Segment in Cortical Principal Neurons Is Caused by the Na − K − 2Cl Cotransporter NKCC1. J. Neurosci. *28*, 4635 − 4639. 10.1523/JNEUROSCI.0908-08.2008.

46. Chamma, I., Chevy, Q., Poncer, J.C., and Lévi, S. (2012). Role of the neuronal K-Cl co-transporter KCC2 in inhibitory and excitatory neurotransmission. Front. Cell. Neurosci. *6*. 10.3389/fncel.2012.00005.

47. Báldi, R., Varga, C., and Tamás, G. (2010). Differential distribution of KCC2 along the axo-somato-dendritic axis of hippocampal principal cells: KCC2 distribution along hippocampal principal cells. European Journal of Neuroscience *32*, 1319–1325. 10.1111/j.1460-9568.2010.07361.x.

48. Rinehart, J., Maksimova, Y.D., Tanis, J.E., Stone, K.L., Hodson, C.A., Zhang, J., Risinger, M., Pan, W., Wu, D., Colangelo, C.M., et al. (2009). Sites of Regulated Phosphorylation that Control K-Cl Cotransporter Activity. Cell *138*, 525 − 536. 10.1016/j.cell.2009.05.031.

49. Côme, E., Marques, X., Poncer, J.C., and Lévi, S. (2020). KCC2 membrane diffusion tunes neuronal chloride homeostasis. Neuropharmacology *169*, 107571. 10.1016/j.neuropharm.2019.03.014.

50. Stevens, M., Peigneur, S., and Tytgat, J. (2011). Neurotoxins and Their Binding Areas on Voltage-Gated Sodium Channels. Front. Pharmacol. *2*. 10.3389/fphar.2011.00071.

51. Dib-Hajj, S.D., Black, J.A., and Waxman, S.G. (2015). NaV1.9: a sodium channel linked to human pain. Nat Rev Neurosci *16*, 511−519. 10.1038/nrn3977.

52. Horikawa, K., and Takeichi, M. (2001). Requirement of the juxtamembrane domain of the cadherin cytoplasmic tail for morphogenetic cell rearrangement during myotome development. Journal of Cell Biology *155*, 1297−1306. 10.1083/jcb.200108156.

53. Gomez, L.C., Kawaguchi, S., Collin, T., Jalil, A., Gomez, M. del P., Nasi, E., Marty, A., and Llano, I. (2020). Influence of spatially segregated IP3-producing pathways on spike generation and transmitter release in Purkinje cell axons. Proceedings of the National Academy of Sciences *117*, 11097–11108. 10.1073/pnas.2000148117.

54. Zorrilla de San Martin, J., Trigo, F.F., and Kawaguchi, S. (2017). Axonal GABAA receptors depolarize presynaptic terminals and facilitate transmitter release in cerebellar Purkinje cells. The Journal of Physiology *595*, 7477–7493. 10.1113/JP275369.

55. Hines, M.L., and Carnevale, N.T. (1997). The NEURON Simulation Environment. Neural Computation *9*, 1179–1209. 10.1162/neco.1997.9.6.1179.

56. Herzog, R.I., Cummins, T.R., and Waxman, S.G. (2001). Persistent TTX-Resistant Na+ Current Affects Resting Potential and Response to Depolarization in Simulated Spinal Sensory Neurons. Journal of Neurophysiology *86*, 1351–1364. 10.1152/jn.2001.86.3.1351.

57. Ratté, S., and Prescott, S.A. (2011). ClC-2 Channels Regulate Neuronal Excitability, Not Intracellular Chloride Levels. J. Neurosci. *31*, 15838–15843. 10.1523/JNEUROSCI.2748-11.2011.

58. Gentiletti, D., de Curtis, M., Gnatkovsky, V., and Suffczynski, P. (2022). Focal seizures are organized by feedback between neural activity and ion concentration changes. eLife *11*, e68541. 10.7554/eLife.68541.

59. Takeuchi, A., Tatsumi, S., Sarai, N., Terashima, K., Matsuoka, S., and Noma, A. (2006). Ionic Mechanisms of Cardiac Cell Swelling Induced by Blocking Na+/K+ Pump As Revealed by Experiments and Simulation. Journal of General Physiology *128*, 495–507. 10.1085/jgp.200609646.

60. Botta, P., de Souza, F.M.S., Sangrey, T., De Schutter, E., and Valenzuela, C.F. (2010). Alcohol Excites Cerebellar Golgi Cells by Inhibiting the Na+/K+ ATPase. Neuropsychopharmacol *35*, 1984–1996. 10.1038/npp.2010.76.

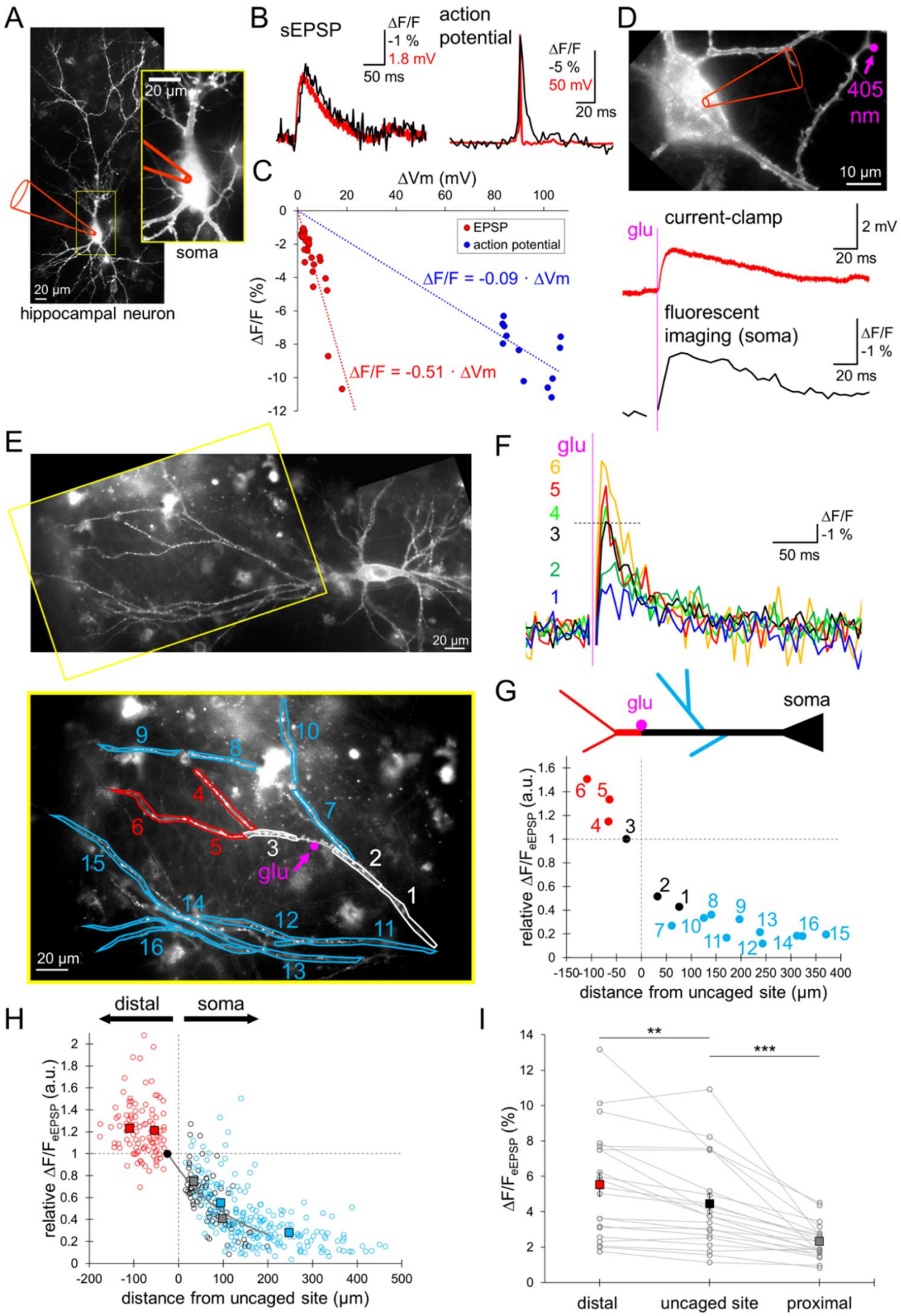
A
20 µm
soma
20 µm
hippocampal neuron
B
sEPSP
ΔF/F
-1 %
1.8 mV
50 ms
action
potential
ΔF/F
-5 %
50 mV
20 ms
C
ΔVm (mV)
EPSP
action potential
ΔF/F = -0.09 · ΔVm
ΔF/F = -0.51 · ΔVm
ΔF/F (%)
D
405
nm
10 µm
glu
current-clamp
2 mV
20 ms
fluorescent
imaging (soma)
ΔF/F
-1 %
20 ms
E
20 µm
F
glu
6
5
4
3
2
1
ΔF/F
-1 %
50 ms
G
glu
soma
relative ΔF/F_eEPSP (a.u.)
distance from uncaged site (µm)
H
distal
soma
relative ΔF/F_eEPSP (a.u.)
distance from uncaged site (µm)
I
**
***
ΔF/F_eEPSP (%)
distal
uncaged site
proximal

913

Figure 1. Direction-dependent EPSP modulation in dendrites by voltage imaging

(A) Fluorescent image of a cultured hippocampal neuron expressing ASAP3β under the whole-cell patch clamp recording.

(B) Representative spontaneous EPSP (left) and action potential (right) in a cultured hippocampal neuron, recorded by ASAP imaging (black) and current-clamp recording (red).

(C) Relative fluorescence changes ($\Delta F/F$) for EPSPs (red, 29 events, 5 cells) and action potentials (blue, 12 events, 3 cells) plotted against the size of membrane potential changes (ΔVm).

(D) Top, single-photon (405 nm) glutamate uncaging around a spine of an ASAP3β-expressing neuron under the whole-cell patch-clamp recording. Bottom, somatic voltage change upon glutamate uncaging recorded by current-clamp (red) or fluorescence imaging (black).

(E) Top, image of an ASAP3β expressing neuron. Yellow rectangular area is expanded below, showing branches used for voltage imaging of local glutamate-evoked EPSPs. Magenta point indicates the location of 405 nm spot laser illumination.

(F) $\Delta F/F_{eEPSP}$ traces at six ROIs (1-6) indicated in E.

(G) Top, Schematic drawing of classification of dendrites (black, dendrite on the way to soma; red, distal branches; blue, bifurcated branches on the way to soma). Bottom, $\Delta F/F_{eEPSP}$ sizes for individual eEPSPs (normalized to that at ROI 3) in a cell (show in E) are plotted against the distance from the uncaged site.

(H) Relative $\Delta F/F_{eEPSP}$ against the distance from the uncaged site (21 cells, red: 102, black: 85, blue: 226 regions based on the categorization shown in G). Square plots indicate averages (± SEM).

(I) Absolute $\Delta F/F_{eEPSP}$ sizes at three categories of location: distal branch, uncaged site, and proximal branch (n = 21 cells, **: $p < 0.01$, ***: $p < 0.001$, paired t-test). Square plots indicate averages (± SEM). See also Figures S1-S3.

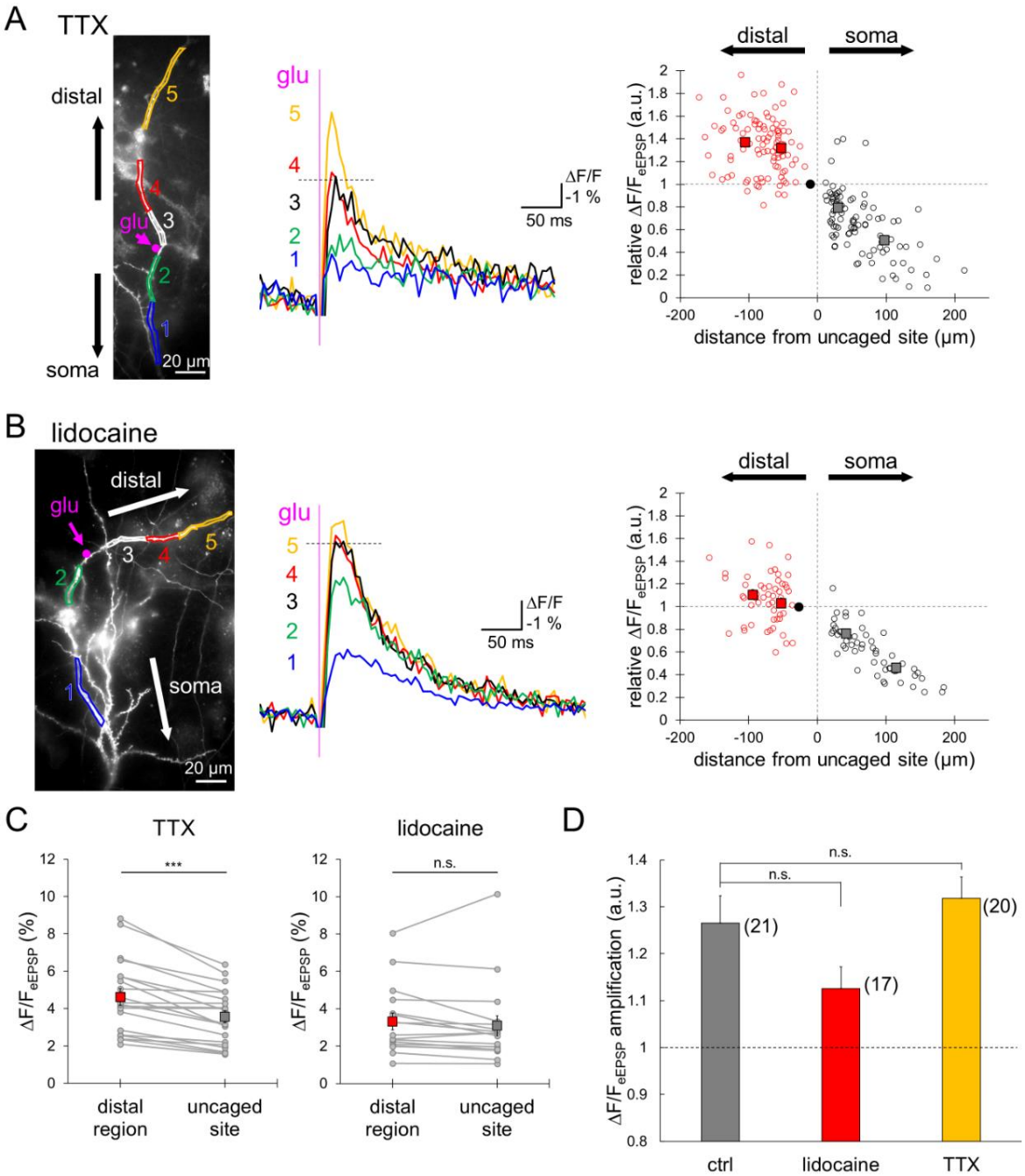

Figure 2. Partial contribution of TTX-resistant Na^+ channels to EPSP amplification

(A) and (B) Left, dendritic segment of interest measured in the presence of TTX (1 μM, A) or lidocaine (5 mM, B). Magenta points indicate the locations of glutamate uncaging. Middle, $\Delta F/F_{eEPSP}$ traces at five ROIs (1-5) indicated in the left. Right, relative $\Delta F/F_{eEPSP}$ plotted against the distance from the uncaged site (20 cells, red: 103, black: 93 regions for A; 17 cells, red: 53, black: 53 regions for B). Square plots indicate averages (± SEM).

(C) Absolute $\Delta F/F_{eEPSP}$ sizes in distal region of dendrites and uncaged sites in the presence of TTX (left, n = 20 cells, *: $p < 0.05$, paired t-test) or lidocaine (right, n = 17 cells, n.s.: not significant, paired t-test). Square plots indicate averages (± SEM).

(D) $\Delta F/F_{eEPSP}$ amplification in distal region with or without TTX and lidocaine (n.s.: not significant, Dunnett's test). Error bars are the SEM.

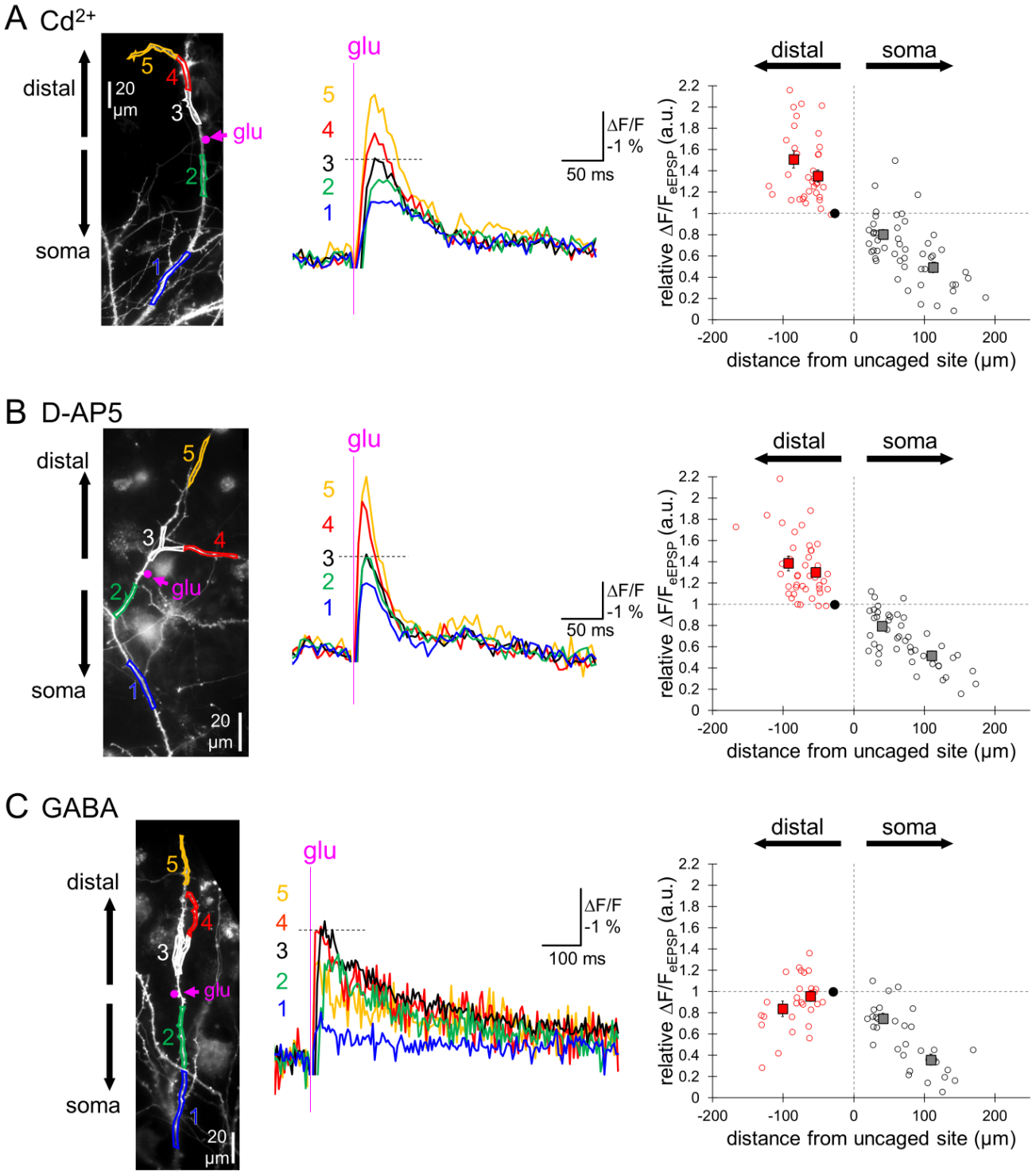
A Cd2+
distal
soma
20 µm
glu
5
4
3
2
1
ΔF/F
-1 %
50 ms
distal
soma
relative ΔF/FeEPSP (a.u.)
distance from uncaged site (µm)
B D-AP5
distal
soma
glu
20 µm
ΔF/F
-1 %
50 ms
distal
soma
relative ΔF/FeEPSP (a.u.)
distance from uncaged site (µm)
C GABA
distal
soma
glu
20 µm
ΔF/F
-1 %
100 ms
distal
soma
relative ΔF/FeEPSP (a.u.)
distance from uncaged site (µm)

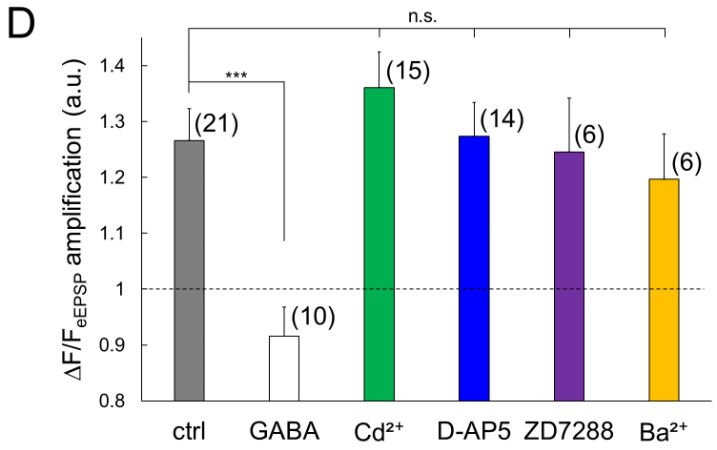
D
n.s.
***
ΔF/FeEPSP amplification (a.u.)
(21)
(10)
(15)
(14)
(6)
(6)
ctrl
GABA
Cd2+
D-AP5
ZD7288
Ba2+

953 **Figure 3. Abolishment of EPSP amplification by GABA-mediated membrane**
954 **shunting, but not by blocking types of cation channel**

955 (A-C) Left, stimulated dendritic segment in the presence of Cd^{2+} (A, 100 μM), D-AP5 (B,
956 100 μM) or GABA (C, 50 μM). Magenta points indicate the locations of glutamate
957 uncaging. Middle, $\Delta F/F_{eEPSP}$ traces at five ROIs (1-5) indicated in left. Right, relative
958 $\Delta F/F_{eEPSP}$ plotted against the distance from the uncaged site (Cd^{2+}, 15 cells, red: 37,
959 black: 50 regions; D-AP5, 14 cells, red: 42, black: 45 regions; GABA, 10 cells, red: 29,
960 black: 31 regions). Square plots indicate averages (± SEM).

961 (D) Statistical summary of $\Delta F/F_{eEPSP}$ amplification in distal branches with or without GABA
962 (50 μM), Cd^{2+} (100 μM), D-AP5 (100 μM), ZD7288 (100 μM) or Ba^{2+} (30 μM). Dunnett's
963 test, ***: $p < 0.001$, n.s.: not significant. Error bars are the SEM. See also Figure S4.

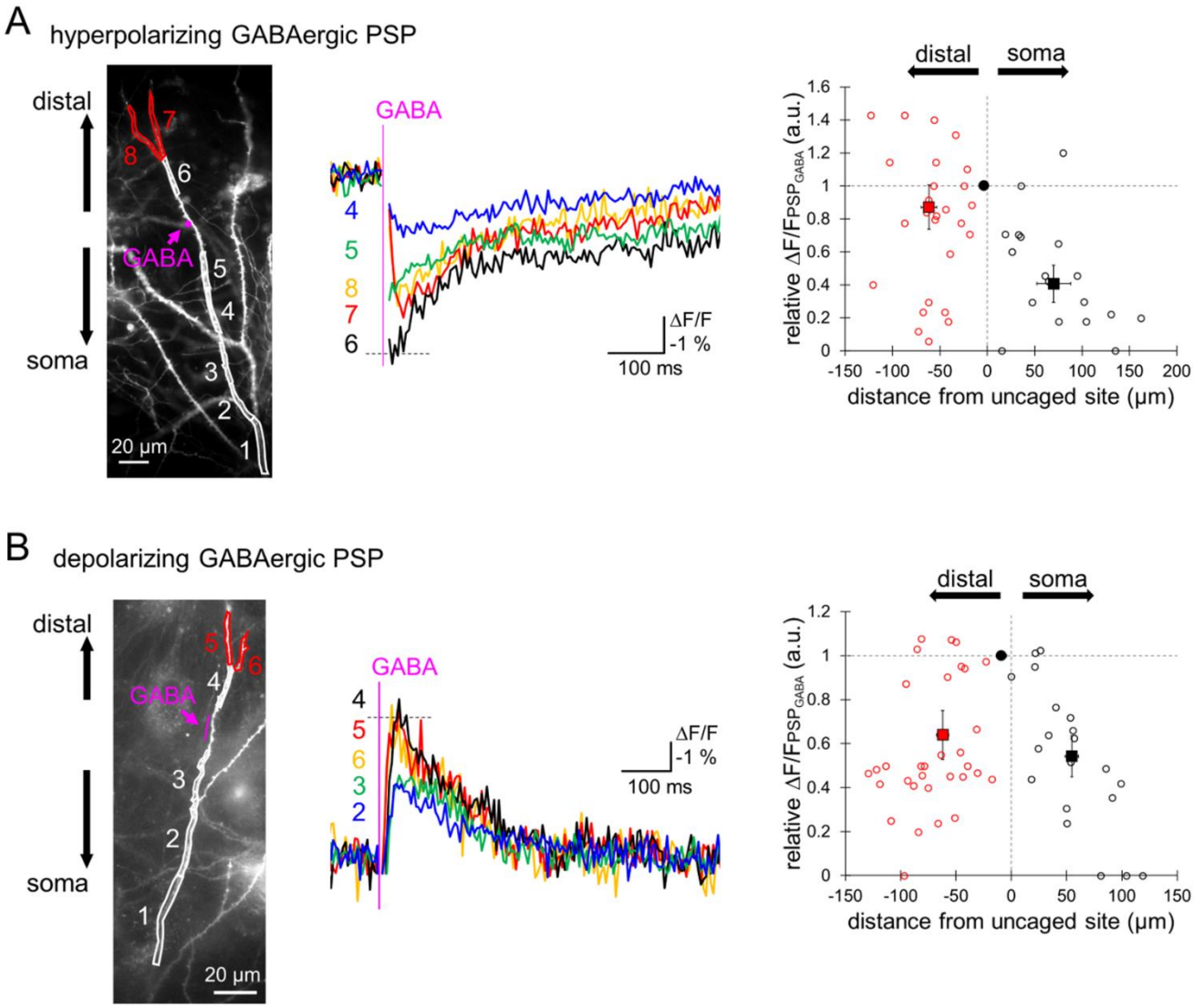

964 **Figure 4. Symmetric attenuative propagation of GABAergic PSPs**

965 (A) and (B) Left, dendritic segments of interest used for voltage imaging upon local
966 GABA-evoked hyperpolarizing (A) or depolarizing (B) postsynaptic potentials (PSP_{GABA}).
967 Magenta point or line indicates the location of GABA uncaging. Middle, ΔF/F for
968 PSP_{GABA} traces at five ROIs (4-8 for A, 2-6 for B) indicated in the left image. Right,
969 relative ΔF/F for PSP_{GABA} is plotted against the distance from the uncaged site (6 cells,
970 red: 25, black: 18 regions for A, 8 cells, red: 33, black: 20 regions for B). Square plots
971 indicate averages (± SEM). See also Figure S5.

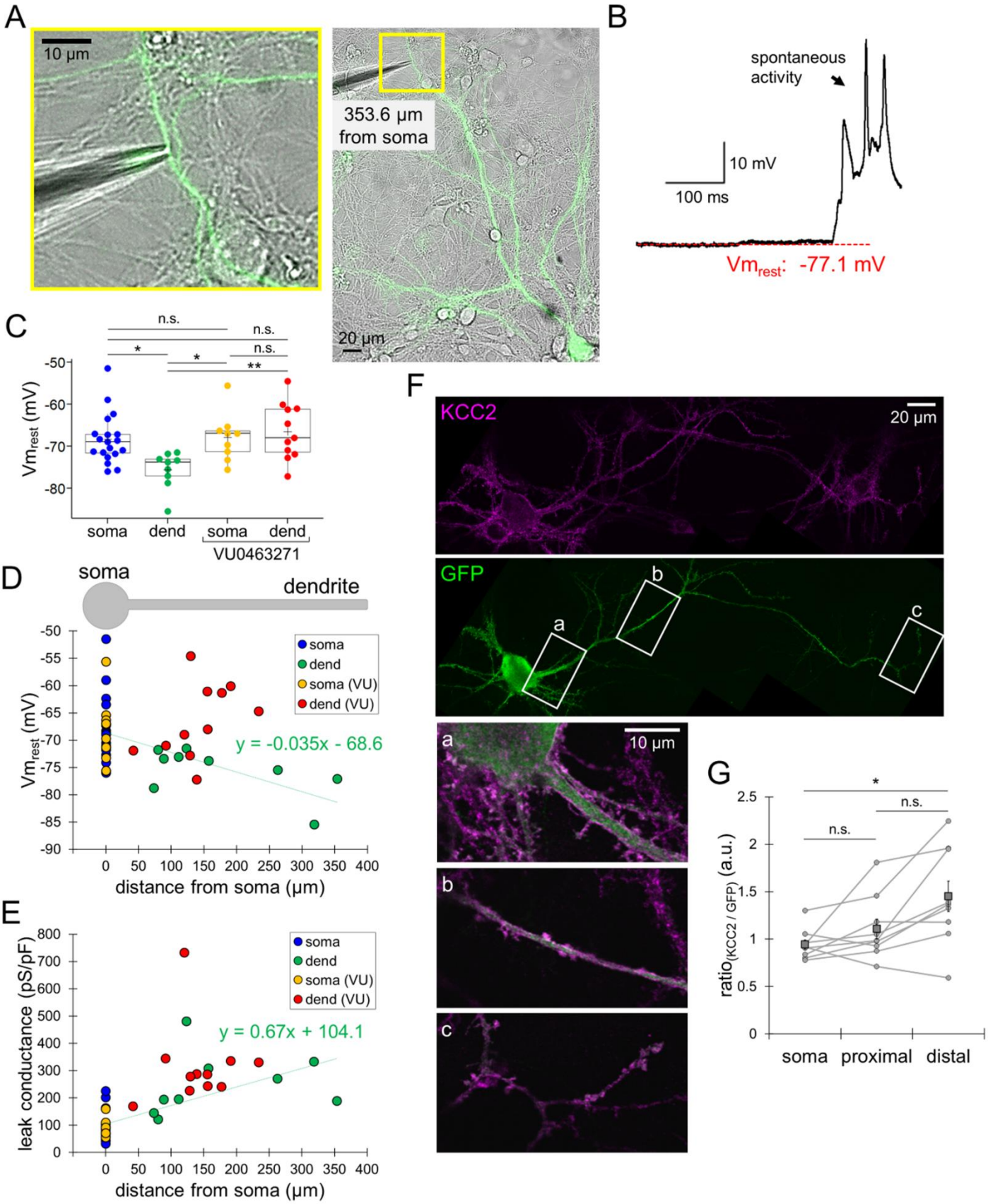
A
10 µm
353.6 µm
from soma
20 µm
B
spontaneous
activity
10 mV
100 ms
Vm$_{rest}$: -77.1 mV
C
n.s.
n.s.
n.s.
*
*
**
Vm$_{rest}$ (mV)
-50
-60
-70
-80
soma
dend
soma
dend
VU0463271
D
soma
dendrite
soma
dend
soma (VU)
dend (VU)
y = -0.035x - 68.6
Vm$_{rest}$ (mV)
distance from soma (µm)
E
soma
dend
soma (VU)
dend (VU)
y = 0.67x + 104.1
leak conductance (pS/pF)
distance from soma (µm)
F
KCC2
20 µm
GFP
a
b
c
10 µm
G
*
n.s.
n.s.
ratio$_{(KCC2 / GFP)}$ (a.u.)
soma
proximal
distal

972

973 **Figure 5. $[Cl^-]_{in}$-dependent more negative membrane potential in dendrites**

974 (A) Image of direct patch-clamp recording from an EGFP-expressing dendrite (right) and
975 magnified view of the patched branch in yellow (left).

976 (B) V_m trace recorded from a dendritic branch (shown in A).

977 (C) Somatic (blue, n = 19 cells) and dendritic (green, n = 9 cells) Vm_{rest} without or with
978 10 μM VU0463271 (soma: yellow, n = 9 cells; dendrite: red, n = 11 cells). Tukey test,
979 *: $p < 0.05$, **: $p < 0.01$, n.s.: not significant.

980 (D) and (E) Vm_{rest} (D) and leak conductance (E) plotted against the distance from soma.
981 VU : in the presence of VU0463271.

982 (F) Images of immunostained KCC2 (magenta, top) in a GFP-labeled hippocampal
983 neuron (green, middle). Three rectangular areas (a - c) are expanded below with
984 color-merged.

985 (G) Ratio of fluorescent intensity of KCC2 to GFP in soma, proximal and distal dendrites
986 (n = 9 cells, *: $p < 0.05$, n.s.: not significant, Tukey test). Square plots indicate
987 averages (± SEM).

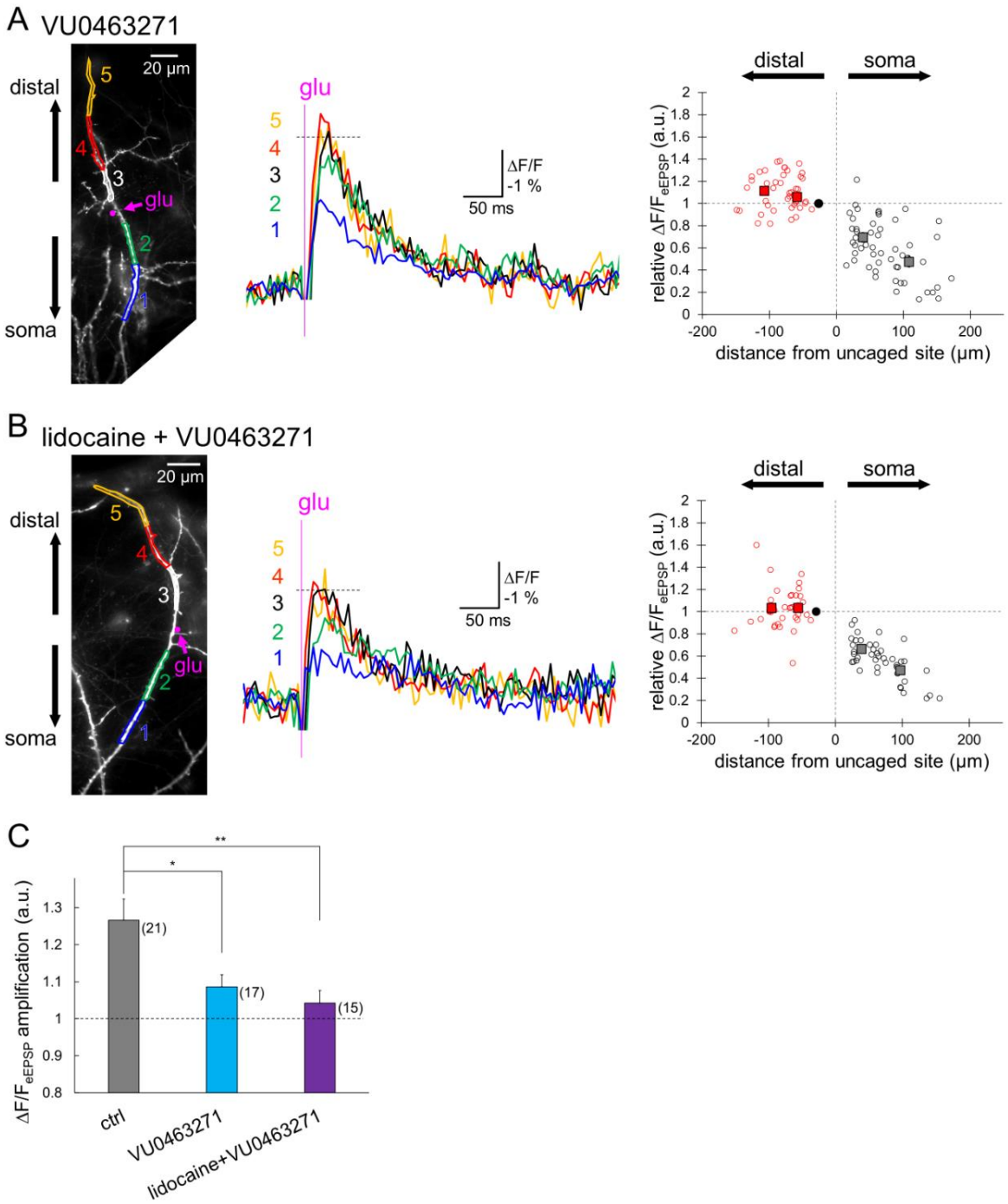

988 **Figure 6. Low $[Cl^-]_{in}$ are involved in EPSP amplification at a dendrite**

989 (A) and (B) Left, stimulated dendritic segment in the presence of VU0463271 (10 μM, A),
990 or lidocaine (5 mM) and VU0463271 (10 μM, B). Magenta points indicate the locations
991 of glutamate uncaging. Middle, $\Delta F/F_{eEPSP}$ traces at five ROIs (1-5) indicated in the left
992 image. Right, relative $\Delta F/F_{eEPSP}$ plotted against the distance from the uncaged site (17
993 cells, red: 44, black: 52 regions for A; 15 cells, red: 38, black: 44 regions for B). Square
994 plots indicate averages (± SEM).

995 (C) Statistical summary of $\Delta F/F_{eEPSP}$ amplification in distal region with or without
996 VU0463271 and lidocaine (*: $p < 0.05$, **: $p < 0.01$, Dunnett's test). Error bars are the
997 SEM.

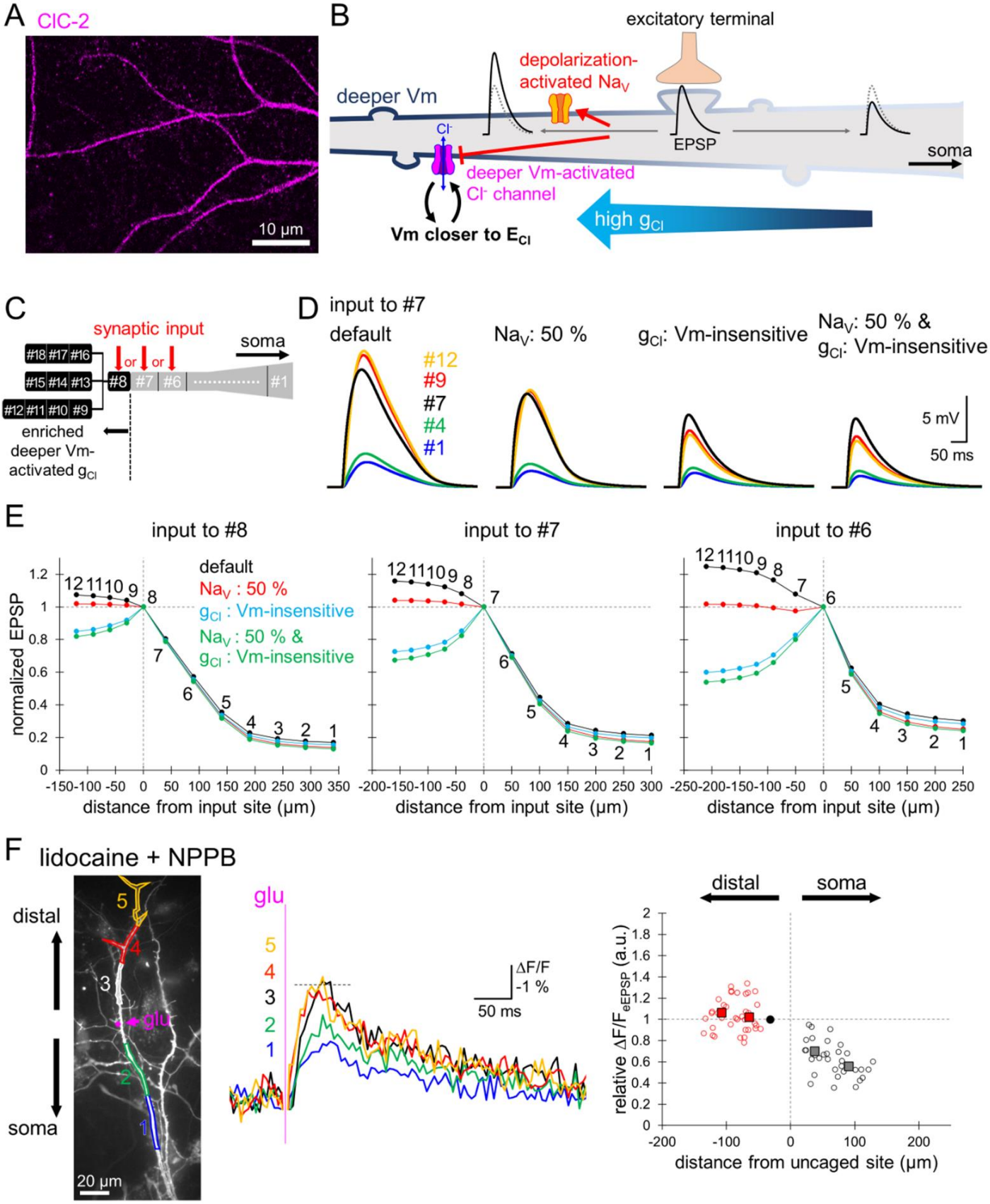
A
ClC-2
10 µm
B
excitatory terminal
depolarization-activated Na_V
deeper Vm
Cl^-
EPSP
soma
deeper Vm-activated Cl^- channel
high g_{Cl}
Vm closer to E_{Cl}
C
synaptic input
soma
#18 #17 #16
#15 #14 #13
#12 #11 #10 #9
#8 #7 #6 #1
or or
enriched deeper Vm-activated g_{Cl}
D
input to #7
default
Na_V: 50 %
g_{Cl}: Vm-insensitive
Na_V: 50 % & g_{Cl}: Vm-insensitive
#12
#9
#7
#4
#1
5 mV
50 ms
E
input to #8
input to #7
input to #6
default
Na_V : 50 %
g_{Cl} : Vm-insensitive
Na_V : 50 % & g_{Cl} : Vm-insensitive
normalized EPSP
distance from input site (µm)
F
lidocaine + NPPB
distal
soma
glu
20 µm
ΔF/F
-1 %
50 ms
distal
soma
relative $\Delta F/F_{eEPSP}$ (a.u.)
distance from uncaged site (µm)

998

Figure 7. Role of Cl^- channels in the low $V_{m_{rest}}$ and local EPSP amplification

(A) Immunostained ClC-2 image in a hippocampal neuron.

(B) Hypothetical model for mechanisms of EPSP amplification in distal dendrites.

(C) Geometric design of a multi-compartment model equipped with the deep V_m-activated Cl^- conductance and the low-threshold Na_V channels. Dendrites are composed of 18 compartments, and an excitatory synaptic input was given at the compartment #6, #7, or #8. See also Table S1.

(D) Simulated EPSP traces (caused at #7) at five representative compartments (#1,4,7,9,12) indicated in C, with or without the 50 % inhibition of Na_V and/or the abolishment of deeper V_m-activated Cl^- conductance change.

(E) Relative amplitude of simulated EPSPs caused at #6 (right), #7 (middle), or #8 (left) plotted against the distance from the input site in 4 conditions of the model.

(F) Left, ASAP3β-imaged dendritic segment in the presence of lidocaine (5 mM) and NPPB (50 μM). Magenta point indicates the location of glutamate uncaging. Middle, $\Delta F/F_{eEPSP}$ traces at five ROIs (1-5) indicated in the left image. Right, relative $\Delta F/F_{eEPSP}$ plotted against the distance from the uncaged site (13 cells, red: 37, black: 34 regions). Square plots indicate averages (± SEM).

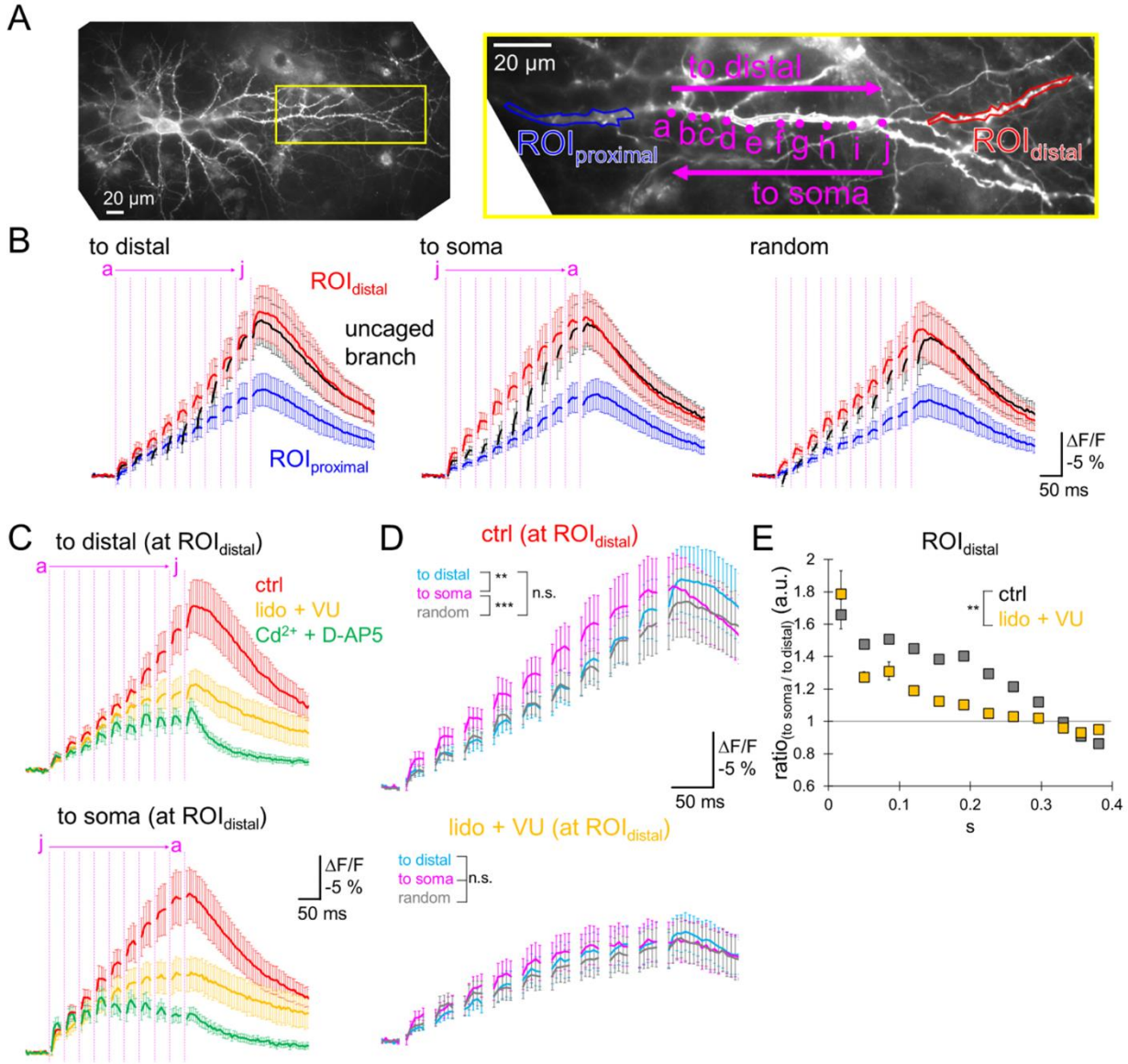

Figure 8. Dynamic spatio-temporal integration of synaptic inputs

(A) Left, image of an ASAP3β-expressing neuron, with yellow rectangular area expanded in right, showing 10 sites of local glutamate uncaging (magenta, 35 ms intervals) in three patterns: to distal (a to j), to soma (j to a) or random.

(B) Averaged $\Delta F/F_{eEPSP}$ traces (± SEM, 17 cells) at three ROIs (uncaged branch: black, proximal: blue, distal: red as indicated in A right) upon three patterns of glutamate uncagings. Magenta lines indicate spot laser illumination.

(C) $\Delta F/F_{eEPSP}$ traces (mean ± SEM) at ROI_{distal} in three conditions: control (red, 17 cells), with lidocaine (5 mM) and VU0463271 (10 µM) (yellow, 13 cells), and with Cd^{2+} (100 µM) and D-AP5 (100 µM) (green, 14 cells).

(D) Comparison of synaptic integration at ROI_{distal} upon three patterns of glutamate inputs in the absence (ctrl, top) or presence of lidocaine and VU0463271 (bottom, **: $p < 0.01$, ***: $p < 0.001$, n.s.: not significant, two-way ANOVA).

(E) Ratio of $\Delta F/F_{eEPSP}$ signals (mean ± SEM) upon opposite directions of glutamate uncagings ("to soma" relative to "to distal") at ROI_{distal} in the absence (ctrl) or presence of lidocaine and VU0463271. **: $p < 0.01$, two-way ANOVA. See also Figure S6.